Solutal convection induced by dissolution

Julien Philippi, Michael Berhanu, Julien Derr,[*] and Sylvain Courrech du Pont
Laboratoire Matière et Systèmes Complexes, Université Paris Diderot, CNRS UMR No. 7057,
10 Rue Alice Domont et Léonie Ducquet, 75205 Paris Cedex 13, France

The dissolution of minerals into water becomes significant in geomorphology when the erosion rate is controlled by the hydrodynamic transport of the solute. Even in the absence of an external flow, dissolution itself can induce a convective flow due to the action of gravity. Here we perform a study of the physics of solutal convection induced by dissolution. We simulate numerically the hydrodynamics and the solute transport in a two-dimensional geometry, corresponding to the case where a soluble body is suddenly immersed in a quiescent solvent. We identify three regimes. At a short timescale, a concentrated boundary layer grows by diffusion at the interface. After a finite onset time, the thickness and the density reach critical values, which starts the destabilization of the boundary layer. Finally, the destabilization is such that we observe the emission of intermittent plumes. This last regime is quasistationary: The structure of the boundary layer and the erosion rate fluctuate around constant values. Assuming that the destabilization of the boundary layer occurs at a specific value of the solutal Rayleigh number, we derive scaling laws for both fast and slow dissolution kinetics. Our simulations confirm this scenario by validating the scaling laws for both onset and the quasistationary regime. We find a constant value of the Rayleigh number during the quasistationary regime, showing that the structure of the boundary layer is well controlled by the solutal convection. We apply the scaling laws previously established to the case of real dissolving minerals. We predict the typical dissolution rate in the presence of solutal convection. Our results suggest that solutal convection could occur in more natural situations than expected. Even for minerals with a quite low saturation concentration, the erosion rate would increase as the dissolution would be controlled by the hydrodynamics.

I. INTRODUCTION

Erosion induced by dissolution and the associated morphogenesis are of particular interest in a geological context. Dissolution is often the dominant erosive process in an area covered by a dissolvable mineral like limestone in karst regions and produces remarkable patterns such as scallops or rillenkarren [1,2]. The three most common dissoluble rocks are salt [halite or sodium chloride (NaCl)], gypsum ($CaSO_4$ and $2H_2O$), and limestone (calcite and $CaCO_3$), whose solubilities in water are, respectively, about 360 g/l, 1.5 g/l, and 2.5 mg/l. It can be inferred that dissolution of these rocks occurs on very different timescales (five orders of magnitude). With the hypothesis of fast kinetics of dissolution, the dissolution rate is often assumed to be controlled by solute transport rather than dissolution kinetics [3,4]. The erosion velocity decreases with the solute concentration at the dissolving interface to vanish when it reaches the saturation concentration. Then diffusive and advective transport of the solute control the erosion dynamics. Inside the ground, if

---

[*]julien.derr@univ-paris-diderot.fr

the rock is porous or fractured, water flows into underground rivers, dissolving progressively the rock and creating dissolution cavities. Complex three-dimensional networks of caves are formed in limestone karst areas, evolving on a timescale typically between 10 000 and 100 000 yr [5]. Understanding the dissolution dynamics of the subsoil is of particular importance to prevent or predict the collapse of large void cavities created by water drainage, leading to the formation of sinkholes [6]. This risk is in particular present where a gypsum stratum is close to the surface, like in Île de France [7].

In nature, hydrodynamic flows enhance solute transport. These flows are often imposed externally, like in the case of an underground river digging a cave. Nevertheless, solute flows can occur without external forcing: buoyancy forces caused by differences in solute concentration can generate a convective flow. Literally analogous to thermal convection, where the density variations are caused by fluid thermal expansion, solutal convection can be triggered by evaporation [8,9] or freezing [10] of salt water or dissolution. Solutal convection induced by dissolution is mostly studied in porous media especially in the context of CO_2 sequestration [11–14]. It can also appear in dissolution cavities filled with water [15,16]. A question of geophysical interest consists in wondering if an external flow is always necessary to achieve considerable erosion of rocks.

Shaping of bodies dissolving in quiescent water due to solutal convection has been reported in several works. Most of them report the formation of patterns. To our knowledge, J. Schürr reports the first observation of these patterns in 1904 during his Ph.d. thesis [17,18] at Clermont-Ferrand (France) under the supervision of Bernard Brunhes. Subsequent studies have been performed from a chemical engineering perspective [19,20] or in a pharmaceutical context [21]. In a geophysical context, Tait and Jaupart [22,23] and then Kerr [24] studied the solutal convection to address precipitation or dissolution in magma chambers. Quantitative measurements of dissolution mass flux and surface patterning were performed with NaCl, KBr, and KCl [25–27] horizontal crystals. This work has been extended recently to inclined bodies [28–30]. Tait and Jaupart [22] and subsequent works infer scalings built on a constant solutal Rayleigh number.

We emphasize that immersing suddenly a dissoluble block into water does not correspond to the classical Rayleigh-Bénard problem. Neither the concentration nor the flux at the boundaries is stationary forced. The standard methods of linear stability analysis cannot be used to predict the onset of the instability. Several theoretical approaches have been proposed to tackle the time-dependent convective instability [31–40], but they rely on strong hypotheses and on arbitrary criteria defining the onset. Although the solutal convective instability corresponds to a nonstationary Rayleigh-Bénard problem, the global dissolution flux is experimentally found to be constant with time [25,29]. The dissolution rate is set by the size of the concentration boundary layer at the dissolving interface, as it is for the temperature boundary layer in turbulent thermal convection. The experimental investigation of this layer remains challenging due to its small size (about 100 μm) and the high concentration gradients, preventing the use of optical techniques.

Here we investigate, by means of numerical simulations, the solutal convection induced by dissolution. At short timescales, we study the development of the boundary layer and the onset of the instability. At longer times, we evidence the establishment of a quasistationary regime and focus on the structure of the associated concentration field. We derive and verify simple scaling laws predicting the onset parameters and the dissolution flux in the regimes where the dissolution is limited by the hydrodynamic transport or by the chemical kinetics. The paper is organized as follows. We detail in Sec. II the theoretical framework used in this study and we derive the associated scaling laws. In Sec. III, for reference, we measure experimentally the onset time of the instability for salt dissolving in saline water. The core of the paper is then dedicated to a two-dimensional numerical simulation of convection. We develop the numerical model in Sec. IV. In Sec. V we detail the temporal evolution of the instability and discuss three distinct regimes. We perform a parametric study of the quasistationary regime in Sec. VI and verify the derived scaling laws. We discuss the possible emergence and growth of dissolution patterns in Sec. VII. In Sec. VIII we address the relevance of the solutal convection induced by dissolution for a natural environment.

II. THEORETICAL FRAMEWORK AND SCALING LAWS

The physical problem of erosion induced by dissolution studied here can be understood as an advection-diffusion problem in the fluid, coupled with a moving solid boundary due to the dissolution [1]. In the following, we discuss the theoretical framework and the validity of the different hypothesis for the typical case of NaCl salt (referred to in the following as salt) dissolving in an aqueous solution.

A. Interface boundary condition at the solid-liquid interface

The dissolution reaction imposes at the solid-liquid interface a solute flux. Considering first-order kinetics, this mass flux Φ is considered to be proportional to the difference between the solute mass concentration at the solid-liquid interface c_i and the saturation mass concentration c_m, $\Phi = \alpha(c_m - c_i)$, where α is the dissolution rate coefficient (always positive) modeling the chemical kinetics of dissolution [41]. We assume a linear relation between the density ρ and mass concentration c of the solution, valid when only one chemical species is in the solution, $c = c_m(\rho - \rho_0)/(\rho_m - \rho_0)$, with ρ_0 the density of the liquid in the absence of solute and ρ_m the density of the liquid at saturation. We also note that, especially for fast dissolving minerals, the kinetics of the chemical solvation reactions have not been precisely documented, at least experimentally. Molecular dynamics simulations at the microscopic scale show a constant dissolution rate of NaCl crystal in the limit of infinitely diluted solvent [42].

The dissolution of the solid results in the receding of the interface

$$-\rho_s \mathbf{v_d} \cdot \mathbf{n} = \alpha(c_i - c_m), \tag{1}$$

where $\mathbf{v_d}$ is the dissolution velocity, $\mathbf{n}$ the normal vector to the interface directed outward from the liquid, and c_i the concentration at the interface. The conservation of the concentration at the interface reads

$$-\rho_s \mathbf{v_d} \cdot \mathbf{n} = -c_i \mathbf{v_d} \cdot \mathbf{n} - D\nabla c|_i \cdot \mathbf{n} + c_i \mathbf{u_i} \cdot \mathbf{n}, \tag{2}$$

where $\mathbf{u_i}$ is the liquid velocity at the interface. The kinematic condition of nonpenetration is written

$$\mathbf{u_i} \cdot \mathbf{n} = \mathbf{v_d} \cdot \mathbf{n}(1 - \chi), \tag{3}$$

where χ is the expansion factor, the ratio between the volumes the solute occupies in the liquid phase and the solid phase. In the quasistatic regime (when $\chi \ll \frac{\rho_s}{c_i}$), and expressed as a function of the fluid density ρ, Eqs. (1)–(3) are rewritten

$$-\rho_s \frac{\rho_m - \rho_0}{c_m} \mathbf{v_d} \cdot \mathbf{n} = \alpha(\rho_i - \rho_m) = -D\nabla\rho|_i \cdot \mathbf{n}, \tag{4}$$

where D is the diffusion coefficient of the solute in the liquid. The quasistatic approximation is reasonable for most practical geological cases. For salt, the saturation concentration is $c_m = 315 \text{ kg m}^{-3}$, the saturation density is $\rho_m = 1200 \text{ kg m}^{-3}$, and the density of the solid salt crystal is $\rho_s = 2163 \text{ kg m}^{-3}$. Then $\rho_s/c_m \sim 10$ while $\chi \lesssim 1$. The dissolution rate depends on the value of the density ρ_i at the interface, which is modified by advection by the hydrodynamic flow in the liquid phase. We neglect the Gibbs-Thomson effect, which increases the dissolution velocity at high curvature (curvature radius smaller than 1 μm) [43,44]. The dissolution process goes with the release or absorption of heat energy because of the change in enthalpy. The dissolution of salt in water is endothermic, which could limit the dissociation rate and affect the concentration saturation value and other involved parameters that are temperature dependent. However, the energy balance is taken to be incidental because first the thermal diffusivity in water is 100 times larger than the mass diffusion coefficient and second because we consider a very large volume of solution acting as a thermostat.

Considering that the characteristic spatial scale of the problem is the concentration boundary layer thickness δ, the mass balance equation (4) is rewritten $\alpha(\rho_m - \rho_i) \approx \frac{D}{\delta}(\rho_i - \rho_b)$, where ρ_b is

the initial density of the solution (bath). From there the effective density difference $\Delta\rho^{\text{eff}}$ created in the boundary layer reads

$$\Delta\rho^{\text{eff}} \equiv \rho_i - \rho_b \approx \frac{\text{Da}}{1 + \text{Da}}\Delta\rho, \tag{5}$$

where $\Delta\rho$ is the maximum density difference $\Delta\rho \equiv \rho_m - \rho_b$ and Da is the dimensionless Damköhler number $\text{Da} = \alpha\delta/D$, which compares the dissolution rate coefficient α and a characteristic diffusion velocity D/δ. When the Damköhler number is large, the dissolution is limited by the diffusion and the concentration at the interface is close to the saturation concentration and $\Delta\rho^{\text{eff}} \approx \Delta\rho$. On the contrary, when the Damköhler number is small, the dissolution is limited by the chemical kinetics. Therefore, the concentration at the interface is close to the bath concentration and $\Delta\rho^{\text{eff}} \approx \text{Da}\Delta\rho$. The coefficient α is not precisely known for most fast dissolving minerals. However, in the case of dissolution of salt in water, using a disk rotating experiment and assuming a first-order dissolution kinetics, Alkattan *et al.* [41] find $\alpha = 5.0 \pm 0.4 \times 10^{-4}$ m s^{-1} at a temperature $T = 25\,°$C. For such a value of α, our simulation will show that Da ~ 10, so the concentration at the interface is close to the concentration at saturation.

B. Scalings for the solutal convection induced by dissolution

1. Onset of convection instability

When putting a block in contact with a solution, the blocks starts dissolving. In a first step, the concentration boundary layer charged in solute grows by diffusion until it reaches a critical thickness δ_{onset} at $t = t_{\text{onset}}$. At this point, the boundary layer becomes unstable due to the gravity action because the concentrated solution is denser. A buoyancy instability develops as shown in our simulations (see Sec. IV). This is analogous to the Rayleigh-Bénard instability where concentration replaces temperature.

The classic theoretical approach to describe the convective instability [45] under the action of the gravity acceleration g relies on the Boussinesq approximation, i.e., the variations of the density with the solute concentration are neglected except for the weight of the fluid particle. Moreover, it supposes that the diffusion coefficient D and the kinematic viscosity ν do not depend on the solute concentration. With these hypotheses, the convective flow between two horizontal plates separated by a distance ℓ occurs in the stationary regime when the Rayleigh number $\text{Ra} = \frac{\Delta\rho^{\text{eff}}g\ell^3}{\eta D}$ exceeds a critical value [22,45], with $\eta = \rho_b\nu$ the dynamic viscosity. The given value depends on the boundary conditions $\text{Ra}_c = 27\pi^4/4 \approx 657.5$ for free-surface boundaries, $\text{Ra}_c = 1708$ for solid walls, and $\text{Ra}_c = 1101$ for mixed conditions. The corresponding wavelengths at the instability threshold are 2.8ℓ, 2.0ℓ, and 2.3ℓ, respectively [45]. In our situation, the geometry is semi-infinite and the phenomenon is not stationary with *a priori* nonconstant concentration at the boundaries. At $t = 0$, the dissolving material is put in contact with the solution, and the initial concentrations and velocity fields are null.

A naive criterion of convection onset consists in basing the Rayleigh number on the boundary layer thickness δ_{onset} as a characteristic length scale. It follows that

$$\delta_{\text{onset}} \approx \text{Ra}_c^{1/3}\left(\frac{\eta D}{\Delta\rho^{\text{eff}}g}\right)^{1/3}, \tag{6}$$

$$\lambda_{\text{onset}} \approx \gamma\delta_{\text{onset}}, \tag{7}$$

where γ is the prefactor linking λ to δ_{onset}. As the boundary layer grows by diffusion during the first step, the onset time of convection scales as $t_{\text{onset}} \approx \delta_{\text{onset}}^2/D$, which gives

$$t_{\text{onset}} \approx \text{Ra}_c^{2/3}\left(\frac{\eta}{\Delta\rho^{\text{eff}}g\sqrt{D}}\right)^{2/3}. \tag{8}$$

Some theoretical works addressed the question of the prefactors. For example, a semianalytical work based on the propagation theory [36,37,46], where part of the dynamics of the base state is taken into account, predicts $t_{\text{onset}} = 7.53(\eta/\Delta\rho g\sqrt{D})^{2/3}$. Later in this article, we perform the full numerical simulation of the problem.

Note that for the practical case of salt dissolution, some of the above hypotheses are questionable. The Boussinesq approximation is valid when the density variations are small, i.e., when $(\rho_m - \rho_b)/\rho_b \ll 1$. For salt $(\rho_m - \rho_b)/\rho_b \approx 0.2$. Moreover, the dynamic viscosity η increases with c from 1.002×10^{-3} to 1.990×10^{-3} Pa s (saturated solution) [47]. The diffusion coefficient is almost independent of concentration with a maximal variation of 7% [48].

2. Quasistationary regime of solutal convection

After the onset, the instability develops and concentrated plumes are intermittently emitted in the vicinity of the interface. The solute flux at the interface reaches a constant value on average (see [27,29] and Sec. IV). We refer to this regime as the quasistationary regime of solutal convection.

In the Rayleigh-Bénard problem, the thermal flux is usually written as a diffusive flux through the gap of distance h times the Nusselt number Nu, which is the ratio between the actual flux and the pure diffusive flux. For large gaps it has been found that the Nusselt number scales as $\text{Ra}^{1/3}$, where Ra is the Rayleigh number based on the gap size h [49]. This results in a thermal flux independent of the gap size h but controlled by the boundary layer thickness δ. By analogy, as previously done [25,27], one can derive a scaling law in the quasistationary regime for the dissolution rate. From Eq. (4), the mass flux of dissolved solute Φ scales like $D(c_i - c_b)/\delta_{\text{qs}}$, where δ_{qs} is the thickness of the boundary layer in the quasistationary regime. On this length scale, one can obtain a new value of the Rayleigh number in the quasistationary regime $\text{Ra}^{\text{qs}} = \frac{\Delta\rho^{\text{eff}}g\delta_{\text{qs}}^3}{\eta D}$. It follows that

$$\Phi \approx (\text{Ra}^{\text{qs}})^{-1/3}\frac{c_m}{\rho_m - \rho_0}\left(\frac{gD^2\Delta\rho^{\text{eff}}}{\eta}\right)^{4/3}. \tag{9}$$

Note that the same expression can be found by equating an advective and a diffusive flux [50].

3. Asymptotic laws

Considering the case of fast dissolution kinetics ($\text{Da} \gg 1$) or slow dissolution kinetics ($\text{Da} \ll 1$), we derive a set of simple scalings from Eqs. (6)–(9) that we compare with our numerical simulations in Sec. VI: For the fast dissolving case $\text{Da} \gg 1$ and $\Delta\rho^{\text{eff}} \approx \Delta\rho$,

$$\delta_{\text{onset}} \approx \text{Ra}_c^{1/3}\left(\frac{\eta D}{\Delta\rho g}\right)^{1/3}, \tag{10a}$$

$$\lambda_{\text{onset}} \approx \gamma\,\text{Ra}_c^{1/3}\left(\frac{\eta D}{\Delta\rho g}\right)^{1/3}, \tag{10b}$$

$$t_{\text{onset}} \approx \text{Ra}_c^{2/3}\left(\frac{\eta}{\Delta\rho g\sqrt{D}}\right)^{2/3}, \tag{10c}$$

$$\Phi \approx (\text{Ra}^{\text{qs}})^{-1/3}\left(\frac{gD^2}{\eta}\right)^{1/3}\frac{c_m}{\rho_m - \rho_0}\Delta\rho^{4/3}, \tag{10d}$$

and for the slow dissolving case $\text{Da} \ll 1$ and $\Delta\rho^{\text{eff}} \approx \text{Da}\Delta\rho$,

$$\delta_{\text{onset}} \approx \text{Ra}_c^{1/4}\left(\frac{D^2\eta}{\alpha\Delta\rho g}\right)^{1/4}, \tag{11a}$$
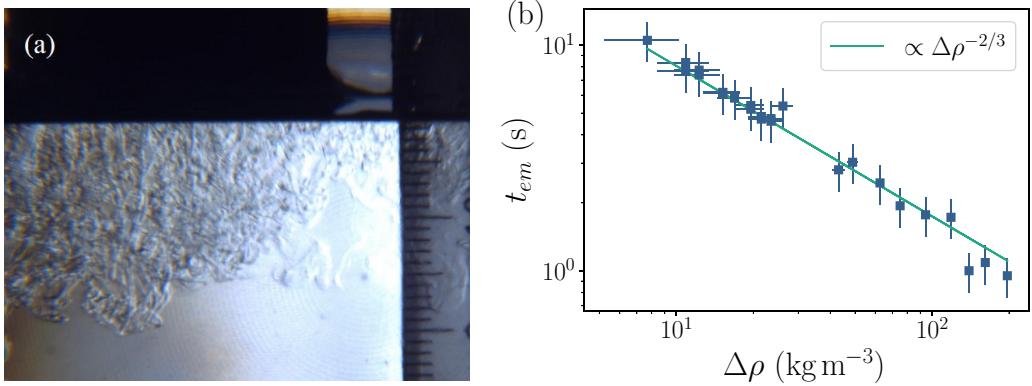
FIG. 1. (a) Shadowgraph image of solutal convective flow. A salt block is put in contact with fresh water and the image is taken 1.25 s after the contact. A graduation corresponds to 1 mm. (b) Emission time t_{em} of the first plume as a function of the density difference $\Delta \rho = \rho_m - \rho_b$, by adjusting the maximal density to $\rho_m = 1195 \text{ kg m}^{-3}$. The straight line indicates the scaling $t_{\text{em}} = K(\eta/\Delta\rho g\sqrt{D})^{2/3}$ with the fitted value $K = 12.8$.

$$\lambda_{\text{onset}} \approx \gamma \, \text{Ra}_c^{1/4}\left(\frac{D^2\eta}{\alpha\,\Delta\rho g}\right)^{1/4}, \tag{11b}$$

$$t_{\text{onset}} \approx \text{Ra}_c^{1/2}\left(\frac{\eta}{\alpha\,\Delta\rho g}\right)^{1/2}, \tag{11c}$$

$$\Phi \approx \alpha\frac{c_m}{\rho_m - \rho_0}\Delta\rho. \tag{11d}$$

In the case of salt (Da $\gg$ 1), the scaling law for the flux Φ in the quasistationary regime (10d) has been observed experimentally by Sullivan *et al.* with a Rayleigh number $\text{Ra}^{\text{qs}} = 133$ [25]. Cohen *et al.* also evidenced this scaling law with $\text{Ra}^{\text{qs}} = 94$ [29]. We propose in the next section to test experimentally with salt the scaling law for t_{onset}.

III. EXPERIMENT: ONSET TIME OF THE CONVECTIVE INSTABILITY FOR SALT

Before addressing the numerical simulations of solutal convection induced by dissolution, which constitutes the major part of this work, we present briefly a few experimental results. Here we put a fast dissolving ionic crystal salt NaCl (Da $\gg$ 1) in contact with a water bath at an initial time $t = 0$. The block is a rectangular cuboid of $5 \times 5 \times 2 \text{ cm}^3$ made of commercial Himalayan pink salt [51].

The water surface is risen progressively and the initial time is detected by the establishment of a meniscus. Later on, we observe the emission of plumes concentrated in the solute. We systematically measure this time t_{em} as a function of $\Delta\rho$ (by varying the concentration of the bath). We visualize the concentration field using a shadowgraph imaging technique. This setup enhances the variations of the optical index, which depends on the solute concentration. This experiment is challenging for small and large $\Delta\rho$ and the accuracy is about 20%. At low salt concentration, the hydrodynamic flow due to the motion of the interface perturbs the measurement. For salt concentration close to the saturation, the optical index contrast is weak.

For pure water, the average t_{em} is found to be equal to 0.95 s. Typically, 0.5-mm-wide plumes sink with a velocity of 15 mm s^{-1}. The shadowgraph in Fig. 1(a) shows a complex structure of entangled plumes corresponding to a turbulent regime of solutal convection. When increasing the concentration of the bath, the emission time increases. For $\rho_b = 1187 \text{ kg m}^{-3}$, we measure an emission time $t_{\text{em}} = 10.5$ s.

The emission time of the first visible plumes t_{em} exceeds the onset time t_{onset} of the convective flow. However, we expect these two timescales to scale similarly. Figure 1(b) shows t_{em} as a function of $\Delta\rho$; t_{em} follows indeed the scaling law derived for t_{onset} [Eq. (10c)]. The best fit gives

$$t_{em} = 12.8(\eta/\Delta\rho g\sqrt{D})^{2/3} \tag{12}$$

when the maximal density is adjusted to $\rho_m = 1195$ kg m^{-3}. The volumetric mass of a saturated solution of salt in pure water was measured to be 1194.1 kg m^{-3} at 25 °C and 1199.1 kg m^{-3} at 15 °C [52].

We take the other parameters to be equal to their value at the concentration of saturation at 20 °C: $D = 1.61 \times 10^{-9}$ m^2 s^{-1} [47] and $\eta = 1.99 \times 10^{-3}$ Pa s [47]. This is consistent with a large Da number and a boundary layer of saturated solution.

The characteristic timescale t_{em} of emission of filaments is thus measurable experimentally and follows the scaling derived for the onset time. However, direct measurements of the onset time t_{onset} and of the typical thickness δ of the concentration boundary layer appear to be unreachable experimentally. Computer simulations are required to access these quantities.

IV. NUMERICAL MODEL

We simulate the development of the instability at early times and the quasistationary dissolution that follows. These simulations enable us to gain access to small times and small distances. They confirm the physical scenario of solutal convection and the associated scaling laws (see Sec. II B 3). They enable us to determine the prefactors that are useful for quantitative predictions.

Furthermore, we can study the transition between the two regimes: the diffusion limited regime and the regime limited by the chemical kinetics. The latter regime, experimentally challenging, due to the long timescales associated, has never to our knowledge been explored so far.

To compute this problem in an efficient way, we have performed numerical simulation of the solutal convective instability with a simplified model. We only solve the coupled equations governing the problem in a two-dimensional domain representing the liquid phase. We assume that the characteristic time of motion of the solid interface is much larger than the hydrodynamic timescale.[1] Therefore, the solid interface at the top of the liquid domain is fixed in the simulations while being a source of solute flux.

We solve simultaneously the incompressible Navier-Stokes equations with the Boussinesq approximation and the advection-diffusion equation for solute concentration. We numerically solve the advection-diffusion equation for the solution density instead of the concentration of solute, which corresponds to a linear relationship between these two quantities. The corresponding set of equations reads

$$\frac{\partial\rho}{\partial t} + (\mathbf{u}\cdot\nabla)\rho = D\Delta\rho,$$

$$\rho_b\left(\frac{\partial\mathbf{u}}{\partial t} + (\mathbf{u}\cdot\nabla)\mathbf{u}\right) = -\nabla p + \nu\rho_b\Delta\mathbf{u} + \rho\mathbf{g}, \quad \nabla\cdot\mathbf{u} = 0,$$

where u, p, and ρ are the velocity, pressure, and density fields, respectively, and ν is the kinematic viscosity. The boundary conditions for velocity and density are (i) a Dirichlet boundary condition $\mathbf{u} = \mathbf{0}$ for the velocity field at the top and at the bottom of the liquid domain because walls are rigid and static and (ii) a Neumann boundary conditions for the density field given by the flux boundary conditions at the solid surface (4) and a no-flux boundary condition at the bottom of the domain.

---

[1]This assumption is stronger than the quasistatic approximation detailed in Sec. II. Both our experiments and the results of our simulations show that it is reasonable, especially for the study of the flow instability.
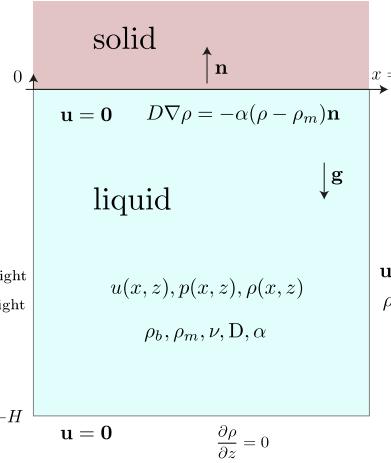
FIG. 2. Representation of the numerical domain with the appropriate boundary conditions.

The latter are written

$$D\boldsymbol{\nabla}\rho|_{z=0} = -\alpha[\rho(z=0) - \rho_m]\mathbf{n}, \qquad \frac{\partial \rho}{\partial z}\bigg|_{z=-H} = 0,$$

where $\mathbf{n}$ is a unit vector pointing outward from the fluid domain. On the left and right sides of the domain, we impose periodic boundary conditions for the velocity and the density fields. Figure 2 displays the geometry of the model.

Using D/α as the characteristic length, D/α^2 as the characteristic time, and ρ_b as the characteristic density, the pertinent dimensionless quantities are written

$$\mathbf{x} = (x, z) = \frac{D}{\alpha}\bar{\mathbf{x}}, \quad t = \frac{D}{\alpha^2}\bar{t}, \quad \rho = \rho_b\bar{\rho}, \quad \mathbf{u} = \alpha\bar{\mathbf{u}}, \quad p = -\rho_b g z + \rho_b\alpha^2\bar{p}.$$

The governing equations in their dimensionless form become

$$\frac{\partial \bar{\rho}}{\partial \bar{t}} + (\bar{\mathbf{u}} \cdot \bar{\boldsymbol{\nabla}})\bar{\rho} = \bar{\Delta}\bar{\rho}, \tag{13}$$

$$\frac{\partial \bar{\mathbf{u}}}{\partial \bar{t}} + (\bar{\mathbf{u}} \cdot \bar{\boldsymbol{\nabla}})\bar{\mathbf{u}} = -\bar{\boldsymbol{\nabla}}\bar{p} + \mathrm{Sc}\,\bar{\Delta}\bar{\mathbf{u}} - (\bar{\rho} - 1)g^*\mathbf{e_z}, \quad \bar{\boldsymbol{\nabla}} \cdot \bar{\mathbf{u}} = 0, \tag{14}$$

where $\mathrm{Sc} = \nu/D$ is the Schmidt number and $g^* = \frac{gD}{\alpha^3}$. Note that we moved the hydrostatic part of the pressure in the gravitational term. The flux boundary condition at the solid surface now reads

$$\bar{\boldsymbol{\nabla}}\bar{\rho} = -[\bar{\rho}(\bar{z}=0) - \bar{\rho}_m]\mathbf{n}, \tag{15}$$

where $\bar{\rho}_m = \frac{\rho_m}{\rho_b}$ is the dimensionless saturation density.

The numerical dimensionless set of equations has been implemented in FREEFEM++ [53,54] and solved with the finite-element methods. The features of our numerical scheme are detailed in Appendix A. Appendix B shows the convergence of the code for several typical runs (see Fig. 12).

With the idea to simulate a semi-infinite domain, we make sure that the height H of the domain is high enough to avoid interactions between the plumes and the bottom boundary. We checked that the results do not depend on H. We have also chosen the width L of the domain in order to obtain an aspect ratio which enables us to correctly determine the characteristic wavelength of the instability but with reasonable computational costs.
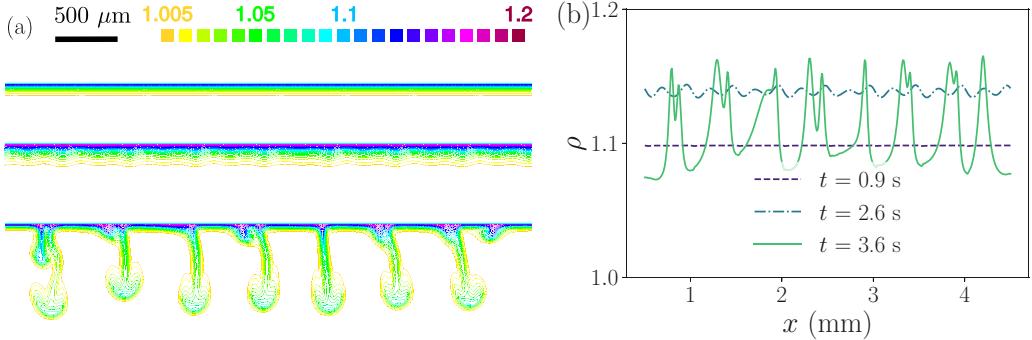
FIG. 3. (a) Snapshots of the simulation (for the case of salt) at different times corresponding to the three regimes discussed in the main text: $t = 0.9$ s (diffusive regime), $t = 2.6$ s (instability regime), and $t = 3.6$ s (plume regime). Each color represents a dimensionless isodensity (see the color scale). (b) Quantitative density profiles at corresponding times. The graph represents the dimensionless density $\rho(x)$ for a fixed distance from the interface ($z = -20$ μm).

V. THE THREE REGIMES OF SOLUTAL CONVECTION

The numerical simulations succeed in reproducing in two dimensions the solutal convective phenomenon observed when a solvable body is suddenly plunged into a water tank, which is by essence nonstationary. Qualitatively, we can identify in the simulations three successive regimes: (i) the diffusive propagation of the concentration front ($t < t_{onset}$), (ii) the growth of the instability ($t_{onset} < t < t_{em}$), and (iii) the emission of plumes and the quasistationary regime of dissolution ($t > t_{em}$).

Snapshots of the density field in Fig. 3(a) and video in [55] show these successive regimes for a typical run. These three successive regimes of dissolution are observable when looking at the density field, the density profile, and the solute flux at the interface Φ. Vertical density profiles as shown in Fig. 4(a) are obtained by averaging horizontally the density field. The density decreases monotonically from its maximum value at the interface to the value of the outer bath. We define the characteristic thickness of the boundary layer as $\delta \equiv 2\Delta z_{half}$, where Δz_{half} is the width of the profile at half maximum. The mass flux Φ of solute entering the fluid phase through the top boundary is

$$\Phi = -\frac{c_m}{\rho_m - \rho_0}\alpha[\langle \rho(z=0)\rangle_x - \rho_m]. \tag{16}$$

The wavelength λ_{onset} and onset time t_{onset} determinations are explained in Appendix C. Figures 3 and 4 represents the data for a typical simulation computed with parameters corresponding to the dissolution of salt in pure water ($\Delta\rho/\rho_b = 0.2$, $\nu = 10^{-6}$ m^2 s^{-1}, $D = 10^{-9}$ m^2 s^{-1}, and $\alpha = 10^{-4}$ m s^{-1}). The dimensionless density can vary from 1 for fresh water to 1.2 for water saturated in salt.

We detail now the three regimes.

(i) Diffusive regime $t < t_{onset}$. At a short timescale $t = 0.2$ s, the density at the interface has increased up to 1.13 at the interface and decreases to the value of the outer bath on a characteristic length scale $\delta = 24.5$ μm. Later on at $t = 0.9$ s, the isodensity curves are still parallel to the interface (Fig. 3), which means that diffusion overcomes gravity. The density profile and the solute flux follow the purely diffusive solution which has been solved analytically by Crank. The concentration field (4) (see [56]) reads

$$c(z,t) = c_m\left\{\text{erfc}\left(-\frac{z}{2\sqrt{Dt}}\right) - \exp\left[-\frac{\alpha}{D}z + \left(\frac{\alpha}{D}\right)^2 Dt\right]\text{erfc}\left(-\frac{z}{2\sqrt{Dt}} + \frac{\alpha}{D}\sqrt{Dt}\right)\right\}. \tag{17}$$
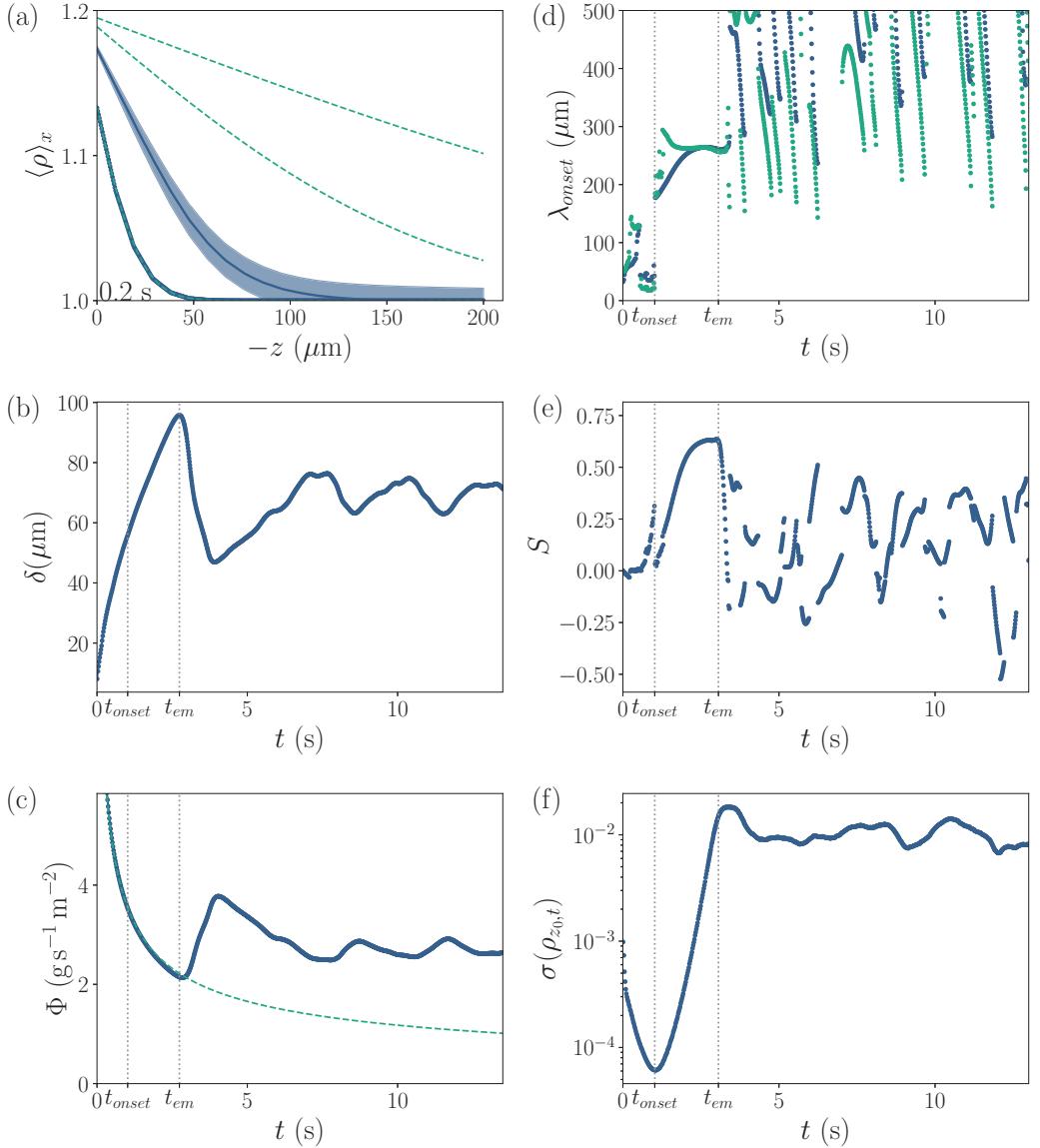
FIG. 4. (a) Spatial density profiles. Blue lines show the result of the numerical simulation for $t = 0.2$ s and $t > 10$ s; the latter is an average in the quasistationary regime. The blue area shows the fluctuation (standard deviation) around the mean profile. These numerical profiles are compared to the analytical diffusive solutions (17) (dashed green lines). From bottom to top, $t = 0.2, 10$, and 50 s. The diffusive theoretical profile describes perfectly the numerical profile at $t = 0.2$ s, but the two profiles differ at later times, in the quasistationary regime. (b) Characteristic thickness δ of the concentrated boundary layer as a function of time ($\delta \equiv 2\Delta z_{\mathrm{half}}$, where Δz_{half} is the width of the density profile at half maximum). (c) Dissolution flux Φ at the interface as a function of time. The blue line indicates the results of the simulation (averaged spatially along the interface), while the dotted green line corresponds to the analytical one-dimensional diffusion solution [obtained via Eq. (17)]. (d) Time evolution of the wavelength determined by autocorrelation, from the first minimum (green dots) and the first maximum (blue dots). (e) Corresponding score S computed as the relative weight of the first peak versus the central peak. (f) Standard deviation σ of the horizontal density profile at the characteristic distance z_0 from the interface where $\langle \rho(z_0) \rangle_x = 0.8 \langle \rho(0) \rangle_x$ (see Appendix C).

(ii) Growth of the instability $(t_{\text{onset}} < t < t_{em})$. At a given time that we define as t_{onset}, the diffusive boundary layer becomes thick enough and starts to destabilize because of gravity. The isodensity curve deforms (see Fig. 3 for $t = 2.6$ s) with an initial wavelength $\lambda = 260$ μm. The amplitude of this density perturbation σ (see Appendix C) exponentially grows in time [Fig. 4(f)].

The solute flux at the interface in Fig. 4(c) moves away from the diffusion solution, showing that the convection has started. However, the convective flow is not yet fully developed.

During the growth of the instability, the solute front still diffuses and the thickness of the boundary layer increases. As a result, the wavelength may also increase with time. This is particularly true for simulations at large viscosity as shown in Fig. 13 in Appendix C.

(iii) Emission of plumes and quasistationary regime $(t > t_{em})$. Finally, the boundary layer destabilizes up to the emission of hydrodynamic plumes at $t = t_{em}$. Plumes sink with a characteristic mushroom-shaped head [see $t = 3.6$ s in Fig. 3(a)]. Then the horizontal density profile shows sharp and strong variations along the x axis [Fig. 3(b)]. The standard deviation of the horizontal density profile σ has reached a maximum and fluctuates in time [Fig. 4(f)].

Plumes are dynamic, move along the interface, and the emission is intermittent. The locations of the plumes at a given time also appear erratic. We measure the characteristic time τ_{plume} between two successive convective plumes [Figs. 5(b) and 5(c)]. For salt in pure water, we measure $\langle \tau_{\text{plume}} \rangle_t = 1.4$ s $\pm$ 0.4 s. This value is very close to the value of t_{onset}, which is the time for the development of the concentration boundary layer before convection. The video in [55] shows the complex motion of plumes, which sink with a typical velocity of 1 cm s^{-1}, consistent with typical experimental values (see Ref. [29] and Sec. III).

At the emission $t = t_{\text{em}}$, the thickness of the boundary layer is maximum. Because the emission of this first plume is almost synchronized, the thickness of the boundary layer falls to a minimum. As a consequence, the concentration gradient in the boundary layer and the dissolution flux increases to a maximum (Fig. 4).

Then, despite the intermittency of plume emissions, the density profile reaches a quasistationary regime with fluctuations around a mean value [see Fig. 4(a)]. Thus, the characteristic thickness of the boundary layer and the solute flux reach quasistationary values; for the case of salt in pure water, $\delta = 69 \pm 4$ μm and $\Phi = 2.7 \pm 0.1$ g s^{-1} m^{-2}. We expect the fluctuations to decrease for a wider system. This regime is of particular importance as it controls the global dissolution dynamics and likely the emergence of patterns when the interface dissolves. This result is consistent with the experiments where a constant dissolution velocity is observed [27,29].

We note that the last regime could be observed due to the finite height of the simulation domain, because of the accumulation of solute at the bottom. However, we always make sure to keep the simulation far from this limit.

Figure 5(a) is a spatiotemporal diagram corresponding to the case of salt in pure water. It displays the evolution of the density at a fixed z, just at the end of the boundary layer, as a function of time t and position x.

First, the density increases homogeneously [regime (i)] until density perturbation appears (light spots in the diagram). They grow [regime (ii)], with a characteristic wavelength until the emission of plumes. The latter are intermittent, i.e., they interact, merge, and die and then new plumes arise [regime (iii)].

VI. SCALING LAWS

In the preceding section we validated our numerical method with the example of salt dissolution in fresh water. We described the main features of solutal convection induced by dissolution. In the following, we confirm the scaling laws drawn in Sec. II B 3. First, we investigate the fast dissolution regime and look at the dependences on the density difference $\Delta\rho$ and the viscosity ν. Then we focus on the dependence on the dissolution rate coefficient α and explore the transition between the fast and the slow dissolution regimes.
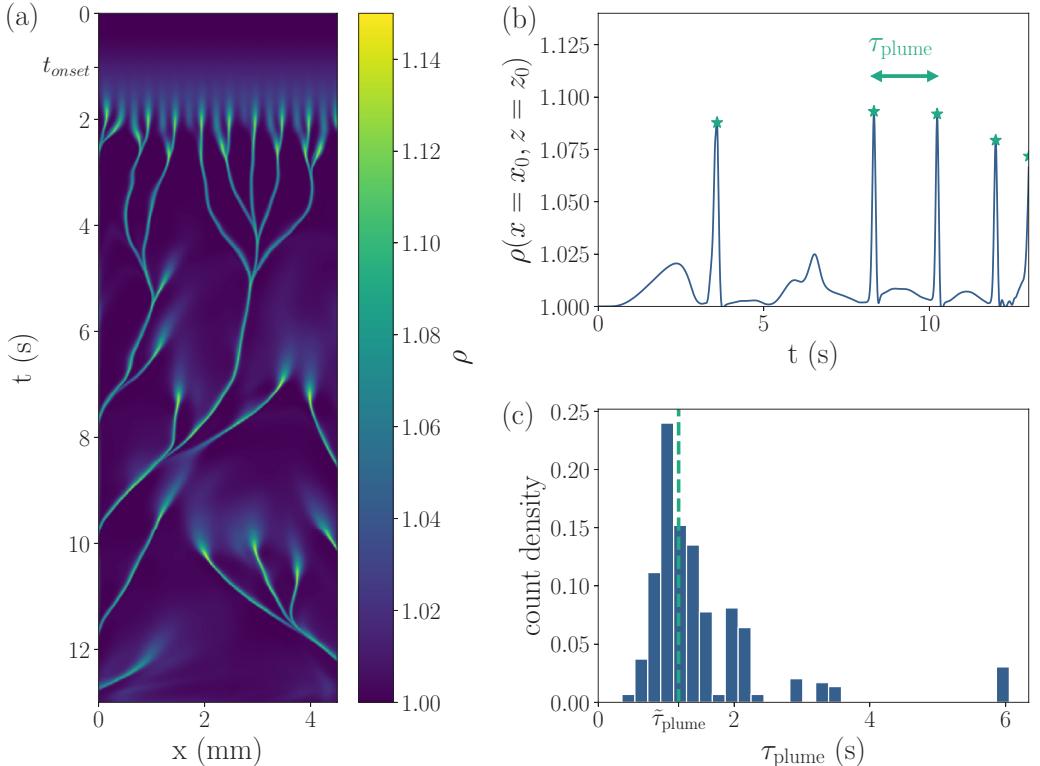
FIG. 5. (a) Spatiotemporal diagram of the density field plotted at $z = -100\ \mu$m. The lateral boundaries are not visible here, as the full size of the simulation was 1 cm. For times smaller than about 1.8 s, the density boundary layer has not yet reached the distance of observation $z = -100\ \mu$m and the convection onset does not appears in this diagram. (b) Time evolution of the density at a particular point ($x_0 = 65\ \mu$m taken arbitrarily) far enough from the interface to probe the hydrodynamic convective plumes ($z_0 = -100\ \mu$m). The stars indicate the sharp peaks in concentration characteristic of the plumes. (c) Histogram of the durations between two successive plumes at $z_0 = -100\ \mu$m for various values of x_0. From this distribution, we characterize the time between two plume emissions by its median and standard deviation: $\tilde{\tau}_{\text{plume}} = 1.4$ s ± 0.4 s.

A. Fast dissolution regime

1. Effect of density difference $\Delta\rho$

We start our investigation by testing the effect of density contrast $\Delta\rho = \rho_m - \rho_b$ on the characteristics of the instability. Simulations are performed, keeping all parameters equal to the case of the salt except the saturation density ρ_m, which we tune from $\rho_m = 1.001\rho_b$ to $\rho_m = 2\rho_b$.

Figure 6(a) display the wavelength λ_{onset} as well as the boundary layer thickness δ_{onset}. Figure 6(b) shows the onset time t_{onset}. For both cases, the theoretical scaling predictions (see Sec. II B 3) are recovered with power laws displaying exponents $-1/3$ and $-2/3$ for λ_{onset} or δ_{onset} and t_{onset}, respectively. The prefactor for t_{onset} is comparable to the one found in the experiment for t_{em}. We find $t_{\text{onset}} = 29.5(\eta/\Delta\rho g\sqrt{D})^{2/3}$, which has the same order of magnitude but is larger than t_{em} measured in experiments with salt [Eq. (12)]. This disagreement for the prefactor could be explained by non-Boussinesq or three-dimensional effects, which are not completely negligible in the experiment of salt dissolution in water.

Figure 6(d) shows the relation between the wavelength λ_{onset} and the thickness of the boundary layer δ_{onset} at the onset. As expected, both quantities are proportional (Sec. II). We find
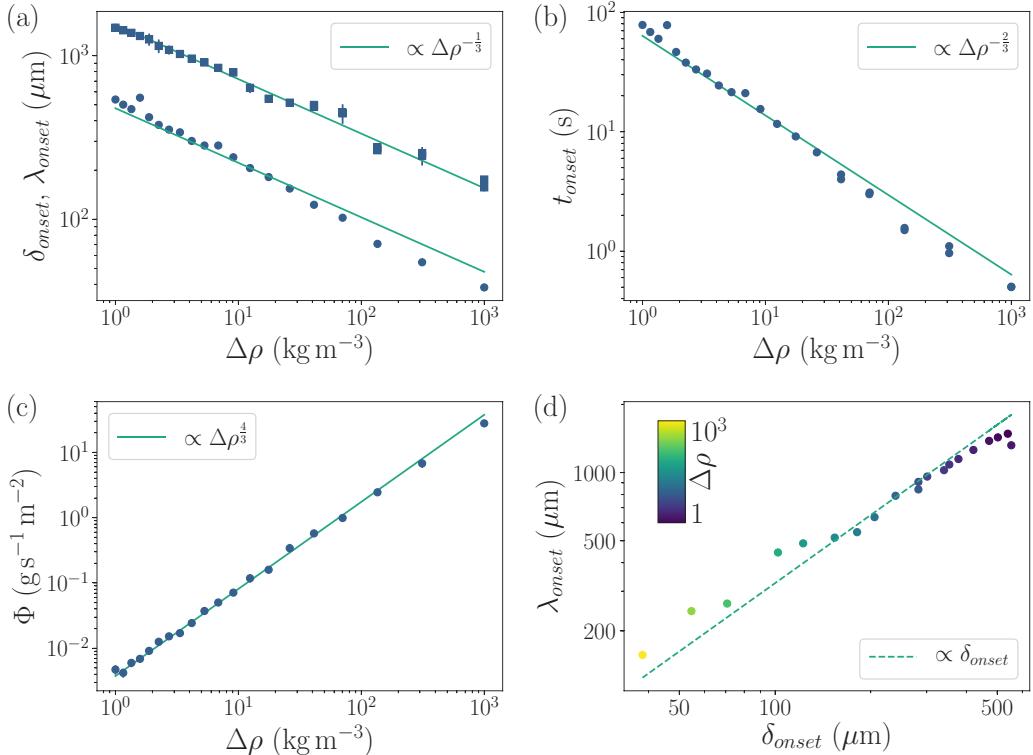
FIG. 6. Influence of density difference $\Delta\rho$. (a) The wavelength at the onset λ_{onset} ($\square$) and boundary layer thickness at onset δ_{onset} ($\circ$), (b) the onset time t_{onset}, and (c) the quasistationary dissolution flux Φ are plotted as a function of density difference $\Delta\rho$. Data are well fitted with the scaling of Eqs. (10b), (10a), (10c), and (10d), respectively. (d) Linear scaling between the wavelength and the thickness of the concentration boundary layer at onset (the proportionality factor is 3.25). The brightness of the symbol indicates the value of $\Delta\rho$ according the scale given in the inset (in $\mathrm{kg\,m^{-3}}$).

$\lambda_{onset} \approx 3.25\delta_{onset}$, which is comparable to the available estimations in the literature. The classic result for Rayleigh-Bénard problem between two plates separated by a distance δ with mixed boundary conditions (nonslipping at one wall and slipping at the other) is indeed $\lambda \approx 2.3\delta$. For the Rayleigh-Taylor instability of a viscous film of thickness δ above an inviscid fluid and in the limit of vanishing surface tension, one finds $\lambda \approx 2.96\delta$ [57,58]. Another analysis of the Rayleigh-Taylor instability between two viscous fluids of the same dynamic viscosity also gives a similar result: $\lambda \approx 3.71\delta$ [50,59]. Note, however, that the prefactor depends slightly on the way δ_{onset} is measured.

Figure 6(c) shows the dissolution flux Φ averaged over time in the quasistationary regime as a function of the density contrast; Φ scales like $\Delta\rho^{4/3}$ [Eq. (10d)]. Indeed, in this fast dissolution regime, the density at the interface is close to the density of saturation.

2. Effect of viscosity

Here simulations are performed by keeping all parameters equal to the case of the salt except the kinematic viscosity, which we tune from $\nu = 10^{-8}\ \mathrm{m^2\,s^{-1}}$ to $\nu = 3 \times 10^{-5}\ \mathrm{m^2\,s^{-1}}$. Contrary to the other results of the paper, the simulated domain is 2 cm wide and 2 cm high in order to avoid the saturation of the wavelength we observe when the domain is too small. Figures 7(a) and 7(b) show λ_{onset} and t_{onset} as functions of the kinematic viscosity. For both cases, the theoretical scaling
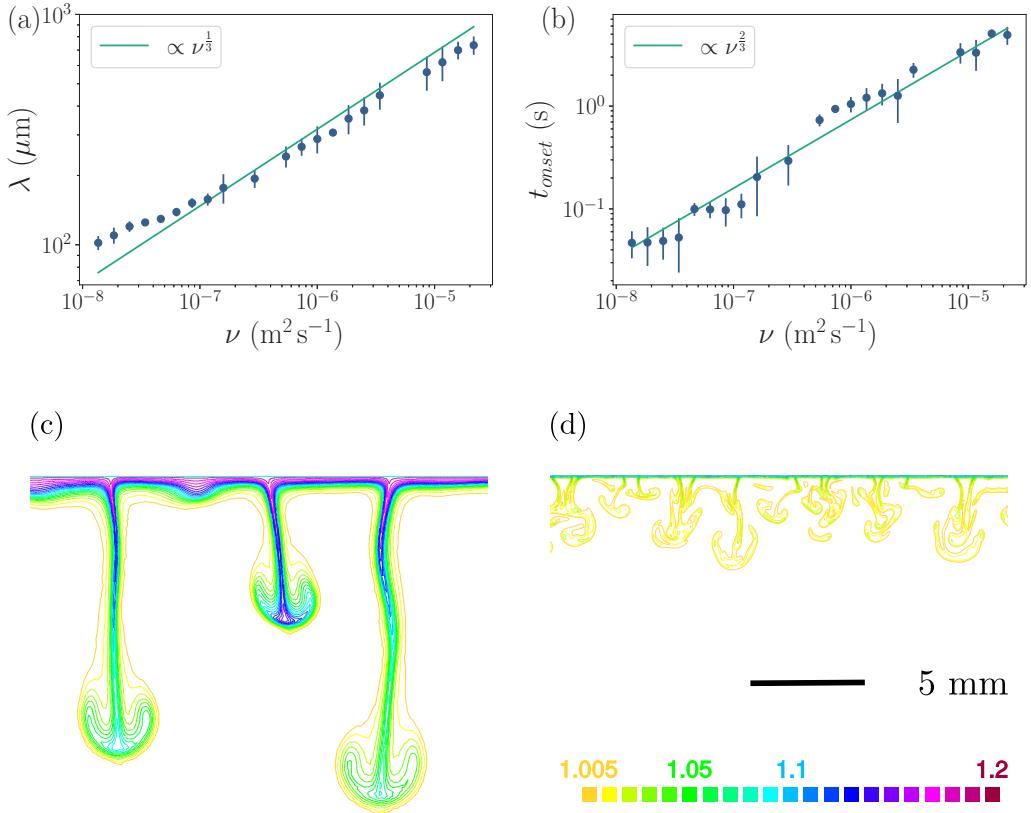
FIG. 7. Influence of the kinematic viscosity ν. (a) Wavelength λ and (b) onset time t_{onset} as a function of the kinematic viscosity ν. Data are well fitted with the scalings for fast dissolution kinetics Da $\gg$ 1 of Eqs. (7) and (8), respectively. Also shown are snapshots of plumes shortly after t_{onset} for (c) $\nu = 10^{-5}$ m^2 s^{-1} and $t \approx 2t_{\text{onset}}$ and (d) $\nu = 10^{-7}$ m^2 s^{-1} and $t \approx 5t_{\text{onset}}$. For both cases, the scale is the same indicated by the 5-mm scale bar. Isovalues for $\frac{\rho}{\rho_b}$ are indicated by the color code.

predictions (see Sec. II B 3) with the 1/3 and 2/3 exponents for λ_{onset} and t_{onset}, respectively, are in good agreement with the numerical simulations.

The shape and the dynamics of plumes depend drastically on the Schmidt number Sc. This is qualitatively evidenced in Figs. 7(c) and 7(d), where the plumes at high Sc are much thinner than the plumes at low Sc, which are more diffuse. However, the robustness of the scalings confirms that the main physics (onset values and dissolution rate) depends on the thickness of the boundary layer but is not sensitive to the detail of the mixing outside the boundary layer.

B. Dissolution rate coefficient α

Here we investigate the role of chemical kinetics of dissolution and the transition between the dissolution kinetics limited regime (Da $\ll$ 1) and the diffusion limited regime (Da $\gg$ 1) by varying the dissolution rate coefficient α while keeping constant all other parameters, which correspond to salt dissolution in water. In particular, the saturation density is kept constant and equals $\rho_m = 1.2$, although α and ρ_m are often correlated. Fast dissolving species have indeed a large saturation concentration and reciprocity. Figure 8 shows the thickness δ_{onset} of the boundary layer, the wavelength λ, and the time t_{onset} at the onset of the instability together with the solute flux Φ as a function of the dissolution rate coefficient α. For large values of α (here when
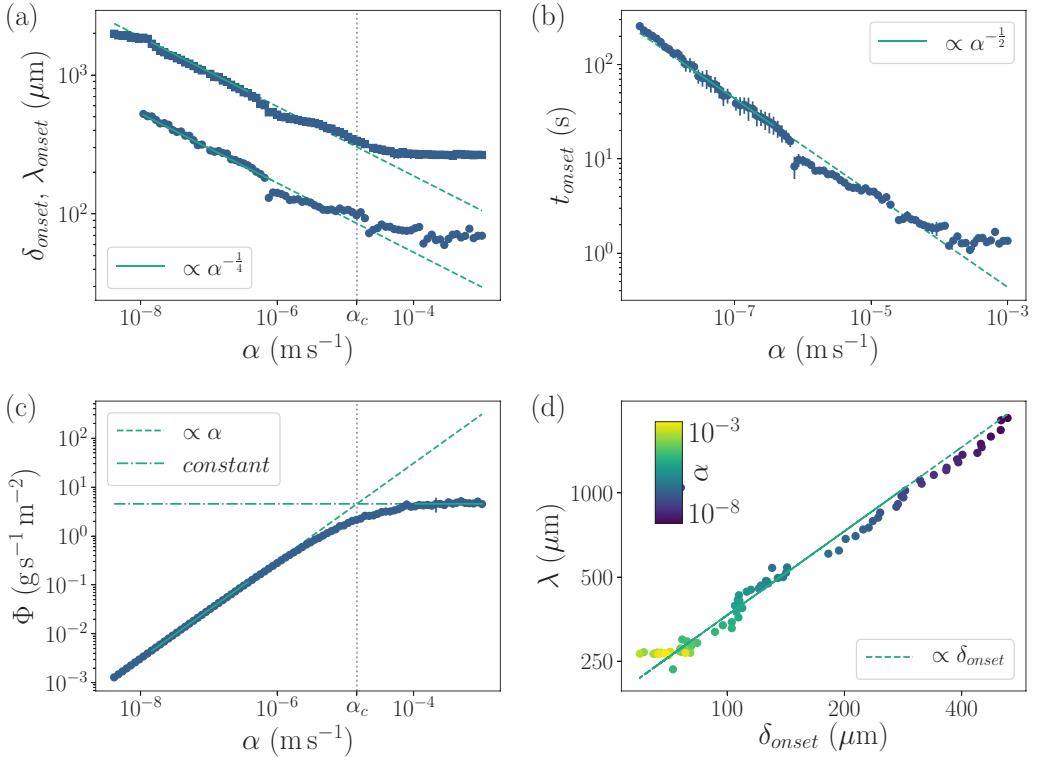
FIG. 8. Influence of the dissolution rate coefficient α. (a) The wavelength at the onset λ_{onset} ($\square$) and boundary layer thickness at onset δ_{onset} ($\circ$), (b) the onset time t_{onset}, and (c) the dissolution flux Φ are plotted as a function of the dissolution rate coefficient α. For $\alpha < 10^{-5}$ m s^{-1}, data are well fitted with the scaling of Eqs. (11b), (11a), (11c), and (11d), respectively. For a high value of α, the data become independent of α. In (c), the crossover value $\alpha_c \approx 1.5 \times 10^{-5}$ m s^{-1} between the slow and the fast dissolving cases is obtained by fitting the two asymptotic regimes. (d) Linear scaling between the wavelength and the thickness of the concentration boundary layer (the proportionality factor is 3.6). The brightness of the symbol indicates the value of α according the scale given in inset (in m s^{-1}).

$\alpha \gg 1.5 \times 10^{-5}$ m s^{-1}), the dissolution process is independent of α. This corresponds to the dissolution limited regime where the concentration at the interface is close to the saturation value [Fig. 9(a)]. For smaller values of α, the dissolution rate plays a role. The diffusion expels the solute more rapidly than it is produced by the dissolution, so the density ρ_i at the interface decreases when α decreases [see Fig. 9(a)]. The buoyancy decreases jointly with the concentration at the interface, so the thickness of the unstable boundary layer increases with the time to develop the instability when α (and ρ_i) decreases. In the limit of vanishing α we observe the concentration at the interface to be asymptotically close to the concentration of the outer bath, as predicted in Sec. II B 2. Then only the dissolution rate and the saturation concentration control the solute flux at the interface, which is proportional to α, as predicted in Eq. (11d). The instability in the fluid is still observed but does not play a role in the global solute flux; however, it will play a role in the pattern formation, as discussed in the next section. In the limit of small α we observe good agreement with the scaling laws we propose, i.e., $\lambda_{\text{onset}} \propto \alpha^{-1/4}$, $\delta_{\text{onset}} \propto \alpha^{-1/4}$, and $t_{\text{onset}} \propto \alpha^{-1/2}$ [Eqs. (11)]. In Fig. 8(d) we verify the expected proportionality between the thickness of the boundary layer and the wavelength at the onset, with $\lambda_{\text{onset}} \simeq 3.6\delta_{\text{onset}}$. In the quasistationary regime, we find that the temporally and
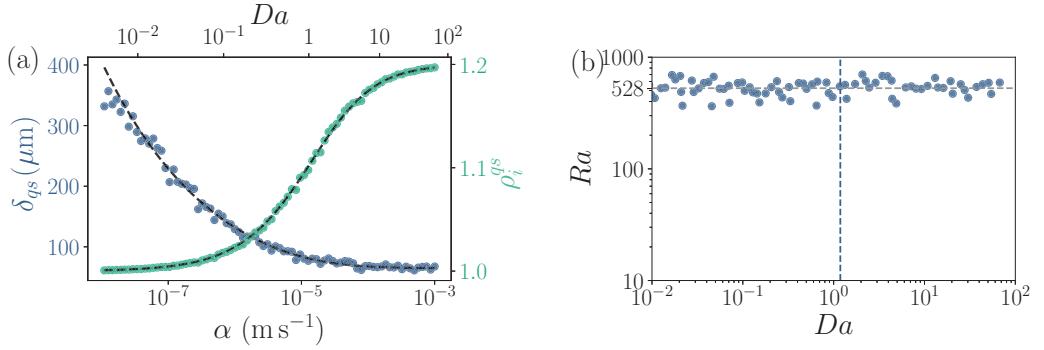
FIG. 9. (a) Evolution of the thickness of the boundary layer δ_{qs} as well as the interface density ρ_i^{qs}, both measured and averaged in the quasistatic regime, as a function of the dissolution rate coefficient α. A fit of these data has been plotted as a dotted line by solving the system (19) described in the text. The Rayleigh number has not been fitted but simply taken as the average value measured (Ra = 528), and we see that the match is very good. (b) Calculation of the Rayleigh number from the measured parameters ρ_i and δ as a function of the Damköhler number.

spatially averaged thickness of the boundary layer is slightly smaller than the onset value, as it is depicted in Fig. 10, where $\delta_{\mathrm{qs}} \simeq 0.83 \delta_{\mathrm{onset}}$ for runs with both variable α and variable $\Delta\rho$.

Extrapolating the scaling laws for the flux Φ in the two regimes (low and high Da), we find a transition for the value $\alpha_c \approx 1.5 \times 10^{-5}$ m s^{-1}, for the set of parameters of salt dissolving in water. Calculating the Damköhler number with δ_{qs}, we find the value of the critical Damköhler number at the transition: Da$_c \approx 1.2$.

C. Constant Rayleigh number independent of α

The flow instability is controlled by the competition between diffusion and gravity to transport the solute. In the quasistationary regime the effective solutal Rayleigh number

$$\mathrm{Ra}^{\mathrm{qs}} = \frac{\Delta\rho^{\mathrm{eff}} g \delta_{\mathrm{qs}}^3}{\eta D}, \tag{18}$$
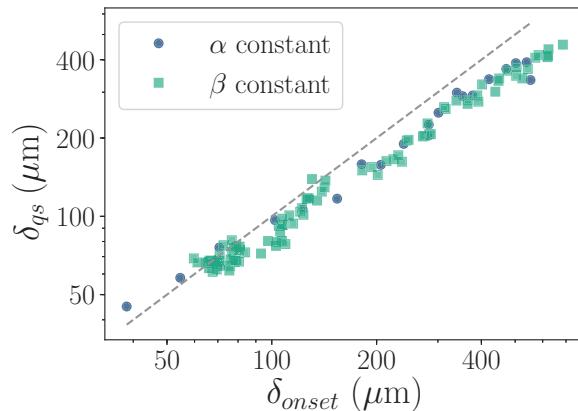
FIG. 10. Comparison of the thickness of the boundary layer at onset δ_{onset} and in the quasistationary regime δ_{qs} for various values of α (blue circles) and $\Delta\rho$ (green squares). The dashed line represents the best linear fit $\delta_{\mathrm{qs}} \approx 0.83 \delta_{\mathrm{onset}}$.

computed with the interface density ρ_i^{qs} and the boundary layer thickness δ_{qs}, is found to be constant and independent of the Damköhler number as shown in Fig. 9(b), where $\mathrm{Ra}^{qs} = 528 \pm 89$. However, the boundary condition at the solid-liquid interface is not fixed but is controlled by the competition between diffusion and chemical kinetics (expressed by the Damköhler number). The concentration at the interface and the thickness of the boundary layer are determined so that they correspond to a constant Rayleigh number. This observation is obtained as an average of the system size. At smaller scale the situation is dynamic: At a given value of x near the dissolving interface the boundary layer thickness increases by diffusion. Once the concentrated boundary layer becomes unstable when $\delta > \delta_{onset}$, the subsequent emission of plumes makes its thickness decrease suddenly below the threshold of instability. Therefore, in the quasistationary regime and for an average size of the dissolving body, the structure of the boundary layer (ρ_i^{qs} and δ_{qs}) corresponds to a constant Rayleigh number because the average thickness of the boundary layer remains δ_{qs} close to δ_{onset}, as shown in Fig. 4(b) or 10.

The Damköhler number Da is not known *a priori*, but one can compute ρ_i and δ from boundary conditions, knowing that the Rayleigh number is constant. The coupled equations read

$$\mathrm{Ra} = \frac{\rho_i - \rho_b}{\rho_b} \frac{g}{\nu D} \delta^3,$$

$$\alpha(\rho_m - \rho_i) = \frac{D}{\delta}(\rho_i - \rho_b). \tag{19}$$

We solved this system as a function of α with $\mathrm{Ra}^{qs} = 528$. The computed result is displayed as dotted lines in Fig. 9(a). The agreement is remarkable despite the approximation $\partial/\partial z \approx 1/\delta$, which confirms the scenario of dissolution at constant Rayleigh number.

This robust value of the Rayleigh number during the quasistationary regime is comparable to the critical values of the Rayleigh number corresponding to the appearance of a convective flow. Using the values obtained at the onset of instability, we find $\mathrm{Ra}_c = 950 \pm 350$. The ratio $\mathrm{Ra}_c/\mathrm{Ra}^{qs}$ is well approximated by $(\delta_{onset}/\delta_{qs})^3 = (1/0.83)^3$. We note that these values of the Rayleigh number depend on an arbitrary way of defining δ (see Sec. V). Therefore, it is delicate to compare our values to the critical values obtained in the literature for the Rayleigh-Bénard convection in the stationary regime [45] (for example, 1100 for mixed boundary conditions) or to the values obtained experimentally using the dissolution flux to estimate the boundary thickness, which are of order 100 [25,29]. In contrast, the critical value of Ra defined using t_{onset} by Eq. (11c) does not rely on an arbitrary estimation of δ. From the fit of Fig. 8(b), we find $\mathrm{Ra}_c = 374$.

VII. DISCUSSION: SPATIAL VARIATIONS OF DENSITY AT THE INTERFACE AND POSSIBLE EMERGENCE OF DISSOLUTION PATTERNS

We saw in previous sections that the global dissolution flux is constant in the quasistatic regime. We address now the spatial variations of the local dissolution flux, which would be responsible for the formation of the patterns observed for dissolving bodies plunged into a solvent [17,18,20,25–28,30]. Analogous dissolution patterns have been observed recently in numerical studies of dissolution in a porous medium [60]. Numerical studies of thermal Rayleigh-Bénard convection with a horizontal melting boundary report also the development of a topography at the solid-liquid interface [61,62]. Melting cavities are separated by cusps, which correspond to the positions of falling plumes. Similarly, in recent dissolution experiments, where the solutal convection creates a pattern, plumes are emitted at the peaks of the topography [28,29].

Spatial variations of concentration at the dissolving interface should induce a dissolution pattern through differential dissolution. Although the interface does not move in our code, we study the space and time fluctuations of the density field at the interface to discuss the emergence of a dissolution pattern resulting from solutal convection. The boundary (4) relates the local interface velocity to the the local value of interfacial solute concentration. The left-hand side of Eq. (4) is
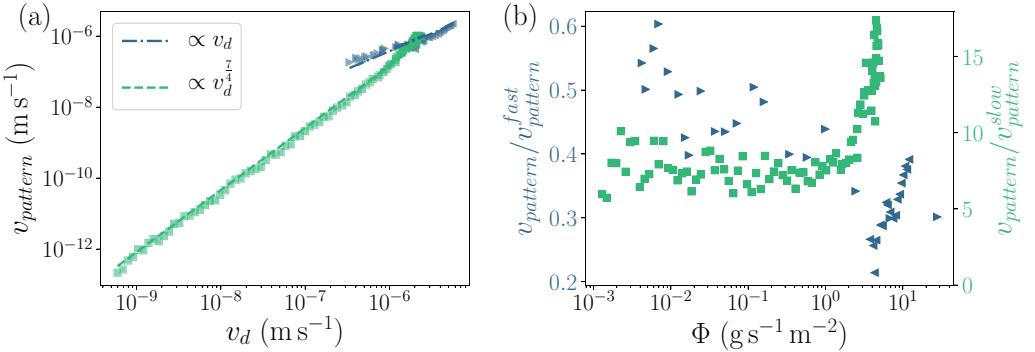
FIG. 11. (a) Relationship between the pattern velocity v_{pattern} and the global dissolution velocity v_d. Green squares correspond to varying values of α. The dashed green line shows the scaling of Eq. (24): $v_{\text{pattern}} = 9.1 v_{\text{pattern}}^{\text{slow}}$. Blue triangles correspond to the fast dissolution regime: $\alpha = 10^{-4}$ m s^{-1} and varying values of $\Delta\rho$ ($\triangleright$) or ν ($\triangleleft$). The dotted blue line displays the scaling of Eq. (25): $v_{\text{pattern}} = 0.38 v_{\text{pattern}}^{\text{fast}}$. (b) Detailed examination of the deviation to the predicted scalings for fast and slow dissolution regimes. While varying α (green squares), the slow dissolution regime scaling in $v_{\text{pattern}}^{\text{slow}} = \text{Ra}^{1/4} (\frac{\eta \rho_s^3 (\rho_m - \rho_0)^3}{g D^2 c_m^3 \Delta\rho^4})^{1/4} v_d^{7/4}$ (with Ra = 500) is followed until a critical flux corresponding to the critical Damköhler number discussed in the preceding section. When we vary $\Delta\rho$ or ν at constant $\alpha = 10^{-4}$ m s^{-1}, one can observe a slight monotonic variation to the fast dissolution scaling: $v_{\text{pattern}}^{\text{fast}} = v_d$. Although $\alpha > \alpha_c$, the value of α is not orders of magnitude larger than α_c, which may be needed to get perfect agreement.

rewritten

$$\mathbf{v_d} \cdot \mathbf{n} = \alpha \frac{\rho_i - \rho_m}{\rho_0 - \rho_m} \frac{c_m}{\rho_s}. \tag{20}$$

We link the typical velocity v_{pattern} at which the pattern emerges (growth velocity) to the spatial fluctuations of $\mathbf{v_d}$ that the spatial fluctuations of the concentration field should induce. Therefore, it corresponds to the standard deviation of the interface velocity

$$v_{\text{pattern}} = 2\alpha \frac{\sigma_{\rho(z=0)}}{\rho_m - \rho_0} \frac{c_m}{\rho_s}, \tag{21}$$

where $\sigma_{\rho(z=0)}$ is the instantaneous standard deviation of the density profile at the interface $\rho(x, z = 0, t)$.

We also define the scalar value v_d as the spatially averaged dissolution velocity, which corresponds to the global dissolution flux. From Eq. (20) it reads

$$v_d = \alpha \frac{\langle \rho(z=0) \rangle_x - \rho_m}{\rho_0 - \rho_m} \frac{c_m}{\rho_s}. \tag{22}$$

As we did for the flux Φ, these quantities are averaged over time in the quasistationary regime.

Figure 11 shows the pattern velocity v_{pattern} as a function of the dissolution velocity v_d for the salt parameters when varying the density difference $\Delta\rho$, the dynamic viscosity ν, or the dissolution rate coefficient α. For fast dissolution kinetics (Da $\gg 1$, varying $\Delta\rho$ or ν), the pattern formation velocity is roughly proportional to the dissolution velocity. Figure 11(b) shows a slight dependence with the flux, but the velocity of pattern formation is always roughly half the speed of the mean interface velocity. For slow dissolution kinetics (Da $\ll 1$, varying α), we find that v_{pattern} scales like $v_d^{7/4}$.

Simple arguments allow us to derive these scaling laws. Between two plumes, the local vertical dissolution flux through the interface matches the divergence of the horizontal advective flux integrated on the thickness of the concentration boundary layer δ, $\Phi \approx \frac{d}{dx}(\delta v_\delta c_\delta)$, where v_δ and

$c_\delta(x)$ are the values of the horizontal velocity and the concentration averaged over the thickness of the boundary layer. Ascribing the differential dissolution to a difference of concentration in the boundary layer only and using the fact that δ and λ are proportional, the previous balance integrated over half a wavelength $\lambda/2$ gives

$$\Delta \bar{c}_\delta \sim \frac{t_{\text{onset}}}{\delta_{\text{onset}}} \Phi, \tag{23}$$

where $\Delta \bar{c}_\delta$ is the characteristic concentration difference inside the boundary layer along the interface and $\frac{\delta_{\text{onset}}}{t_{\text{onset}}}$ is the typical flow velocity in the boundary layer.

By definition, v_{pattern} scales like the characteristic difference of dissolution velocity, so $v_{\text{pattern}} \sim \frac{\alpha}{\rho_s}(\Delta \bar{c}_i)$, where $\Delta \bar{c}_i$ is the characteristic difference of concentration at the interface. For a linear concentration boundary layer, $\Delta \bar{c}_i \sim 2\Delta \bar{c}_\delta$.

In the slow dissolving case, the dissolution flux Φ, t_{onset}, and δ_{onset} are given by Eq. (11c), (11a), and (11d), so we find

$$v_{\text{pattern}}^{\text{slow}} = \text{Ra}^{1/4}\left(\frac{\eta \rho_s^3 (\rho_m - \rho_0)^3}{gD^2 c_m^3 \Delta \rho^4}\right)^{1/4} v_d^{7/4}, \tag{24}$$

where the scaling of pattern formation is written as a function of the global dissolution velocity $v_d = \frac{\Phi}{\rho_s}$. Similarly, in the fast dissolving case, the dissolution flux Φ, t_{onset}, and δ_{onset} are given by Eq. (10c), (10a), and (10d), which gives

$$v_{\text{pattern}}^{\text{fast}} = v_d. \tag{25}$$

These scaling laws agree fairly well with our data. Although the solid interface is fixed in our simulations, these velocities of pattern formation should prevail at least in the early stage, when patterns have small amplitudes.

However, as discussed in Sec. II and commonly reported [1], the hydrodynamic timescales are substantially shorter than those corresponding to the interface evolution. Therefore, to observe the growth of a significant pattern, the lifetime of the concentration variations should be larger than or of the order of the typical time for pattern formation. Thus, pattern formation relies on a time coherent spatial differential density profile at the interface: If the plume positions are uncorrelated in time, the interface should remain flat. For the parameters of salt dissolution in pure water, we find $v_{\text{pattern}} \approx 0.38 v_d$. Liu *et al.* found a similar value in experiments [26]. The typical time lapse between the emission of two plumes at a given location of the boundary layer is $\tau_{\text{plume}} \approx 1.4$ s (Fig. 5); τ_{plume} sets the coherence time of the boundary layer. Over this coherence time, the pattern attains a typical amplitude $v_{\text{pattern}}\tau_{\text{plume}} \approx 10^{-6}$ m, which is about 50 times smaller than the thickness of the boundary layer (see Fig. 4). This small rugosity may stabilize the position of plumes to explain the emergence of patterns in experiments [26–29]. We have performed simulations with a solid interface with peaks. They evidence that spikes at the interface stabilize the plume locations. This offers perspective for future work studying the effect of the topography in the emergence of patterns by simulating the same problem with a moving interface.

VIII. CONCLUSION

Motivated by the geophysical relevance of erosion by dissolution, we performed an extensive numerical study of the solutal convection induced by dissolution, which occurs when immersing a horizontal dissolving body in a quiescent solvent. Through the example of salt dissolving in water, we described the three regimes of the convection driven by dissolution. First was the diffusive regime, where the concentration boundary layer grows by diffusion until the thickness and the density reach critical values at a finite time, the onset time. In the second regime, the boundary layer destabilizes because of the buoyant flow and eventually leads to the emission of plumes. The third regime of plumes emission corresponds to a quasistationary regime where the structure of the boundary layer and the dissolution rate fluctuate around constant values. In this established

TABLE I. Geological application of our numerical results in the cases of NaCl salt, gypsum, and limestone. The fits in Figs. 6(c) and 8(c) give the prefactors for onset characteristics. In the fast dissolution regime, we found $t_{onset} \approx 29.2(\frac{\eta}{g\sqrt{D}})^{2/3}\Delta\rho^{-2/3}$, $\delta_{onset} \approx 10.2(\frac{\eta D}{g})^{1/3}\Delta\rho^{-1/3}$, and $\Phi \approx 0.11(gD^2/\eta)^{1/3}\frac{c_m}{\rho_m-\rho_0}\Delta\rho^{4/3}$. In the slow dissolution regime, we found $t_{onset} \approx 19.3(\frac{\eta}{\Delta\rho g})^{1/2}\alpha^{-1/2}$, $\delta_{onset} \approx 6.25(\frac{D^2\eta}{\Delta\rho g})^{1/4}\alpha^{-1/4}$, and $\Phi \approx 0.98\frac{c_m}{\rho_m-\rho_0}\Delta\rho\alpha$. The erosion velocity is $v_d = \frac{\Phi}{\rho_s}$. The chosen parameters for salt are $D = 1.61 \times 10^{-9}$ m^2 s^{-1}, $\nu = 1.66 \times 10^{-6}$ m^2 s^{-1} (saturated concentration), $\rho_m = 1.2$, $\Delta\rho = 200$ kg m^{-3}, $c_m = 315$ kg m^{-3}, $\alpha = 5.0 \times 10^{-4}$ m s^{-1} [41], and the solid density $\rho_{salt} = 2170$ kg m^{-3}. The parameters for gypsum are [3] $D = 1.0 \times 10^{-9}$ m^2 s^{-1}, $c_m = 2.04$ kg m^{-3}, $\Delta\rho = 2.58$ kg m^{-3}, $\alpha = 2.7 \times 10^{-6}$ m s^{-1}, and the solid density $\rho_{gypsum} = 2320$ kg m^{-3}. We take for the viscosity the value for fresh water $\nu = 10^{-6}$ m^2 s^{-1}. For limestone, the chemical reaction of dissolution involves the partial pressure in CO$_2$ and depends on the *pH*. Moreover, the dissolution rate is not linear with the concentration in ions Ca^{2+}, due to an inhibition phenomenon at high concentration. We take $\alpha \approx 3 \times 10^{-6}$ m s^{-1} [63], which constitutes a higher bound in natural conditions. The other parameters for the limestone are $D = 1.4 \times 10^{-9}$ m^2 s^{-1}, the density at saturation in conditions of high CO$_2$ pressure is $\rho_m = 1.000\,312$ kg m^{-3} [63] and so $\Delta\rho = 3.12 \times 10^{-1}$ kg m^{-3} and the solid density $\rho_{limestone} = 2711$ kg m^{-3}. Due to the weak solute concentration, the viscosity is the one of fresh water $\nu = 10^{-6}$ m^2 s^{-1}. We choose also $c_m = 0.057$ kg m^{-3} [63].

Mineral	Dissolution regime	t_{onset} (s)	δ_{onset} (μm)	Da	D/δ (μm s^{-1})	Φ (g m^{-2} s^{-1})	v_d
salt NaCl	fast kinetics	2.2	113	35	14	5.1	74 m yr^{-1}
gypsum	fast kinetics	33.7	349	0.93	2.9	2.9×10^{-2}	39 cm yr^{-1}
gypsum	slow kinetics	74	389	1.0	2.6	5.4×10^{-3}	7.3 cm yr^{-1}
limestone	fast kinetics	123	787	1.7	1.8	1.0×10^{-3}	1.2 cm yr^{-1}
limestone	slow kinetics	202	756	1.62	1.8	1.7×10^{-4}	0.2 cm yr^{-1}

regime, as for the onset of the instability, the solutal Rayleigh number is constant when calculated with the actual density at the interface and the thickness of the concentration boundary layer. This constant value of the Rayleigh number sets the scaling laws that grasp the dynamics of convective dissolution. Varying the density difference, the viscosity, and the characteristic dissolution rate, we confirm the physical picture and the scaling laws for the fast dissolving materials (Da $\gg$ 1) and derive and verify the scaling laws for slow dissolving materials (Da $\ll$ 1). For such materials, the solute concentration at the solid interface is smaller than the concentration of saturation, but still the effective Rayleigh number is constant and equals approximately 500 in the quasistationary regime. This is of particular importance when considering dissolution of geological materials such as gypsum or limestone. Table I summarizes for NaCl salt, limestone, and gypsum the onset time t_{onset} (s), the thickness of the boundary layer at the onset δ_{onset}, the Damköhler number Da, the characteristic velocity D/δ for which the advection by an external flow dominates the diffusion, the dissolution flux Φ, and the erosion velocity v_d. For salt, our predictions match the orders of magnitude found in experiments: onset time of the order of 1 s (see our experiment in Sec. III) and fluxes of the order of a few g m^2 s^{-1} (see [29]). If salt is a fast dissolving material, limestone and gypsum appear to stand at transitional values of the Damköhler number. The occurrence of solutal solution induced by dissolution is of prime importance in predicting the dissolved mass of minerals as a function of time. In the presence of diffusion alone, the flux vanishes slowly with time, as the concentration boundary layer becomes more and more thick. In contrast, once the quasistationary regime of solutal convection characterized here has been reached, the erosion velocity remains constant, which implies a significantly higher amount of dissolved material. This point is crucial specifically in the case of the development of dissolution cavities in gypsum strata which can lead to the appearance of sinkholes at the surface [6,64–66]. In nature, an external flow could inhibit the solutal convection. If the velocity of an externally forced flow, in the boundary layer, is larger than the characteristic velocity D/δ, the external flow would overcome the solutal convection to transport the solute. However, in the case of quiescent water, although the dissolution rates can be

weak even with a Damköhler number of order one, the solutal convection undoubtedly takes place after a few seconds to a few tens of seconds only, making this mode of dissolution worth considering on geological times.

APPENDIX A: NUMERICAL METHODS

All the numerical simulations were performed with the open-source code FREEFEM++ [67] (see also the paper of Hecht [53] for details). FREEFEM++ is a code solving partial differential equations using the finite-element method. One of the particularities of this code is that the problem to solve is described by its variational formulation. In this Appendix we provide some details about the weak form of the dimensionless system (13)–(15) implemented in the code.

1. Weak form of the governing equations of the problem

a. Temporal discretization of the momentum equation and introduction of the FREEFEM $+ +$ *operator* convect

The main difficulty in the determination of the weak form of the equations governing this problem comes from the nonlinear convective term. However, it is possible with FREEFEM++ to take it into account with an operator called convect. This operator appears explicitly in the weak formulation of the problem implemented in the FREEFEM++ code. Obviously, due to this operator specific to the code, the variational formulation we propose here does not correspond to those we found in [68,69].

In order to properly introduce the convect operator, we can start by writing the time discretization of the momentum equation. This involves the velocity at times n and $n+1$, pressure at time $n+1$, and density at time n. Indeed, we compute the velocity and the pressure fields with the momentum equation for the density given at the previous time step. This difference lies in the timescale separation between hydrodynamic and advection-diffusion phenomena. Therefore, we obtain from Eq. (14) the discretized momentum equation (after dropping the overbars)

$$\frac{1}{\tau}\big(u_i^{n+1} - u_i^n \circ X_i^n\big) + \frac{\partial p^{n+1}}{\partial x_i} - \mathrm{Sc}\Delta u_i^{n+1} + (\rho^n - 1)g^*\delta_{i2} = 0,$$

where τ is the time step of the discretization. The term $u_i^n \circ X_i^n(x)$ could be approximated by the term $u_i^n[x - u_i^n(x)\tau]$, which we use to define the FREEFEM++ convect operator $\mathtt{convect}(\mathbf{u}^n, -\tau, u_i^n) := u_i^n[x - u_i^n(x)\tau]$.

b. Weak form of Navier-Stokes equations

We consider here the discretized dimensionless Navier-Stokes equations written with the operator convect,

$$\frac{\partial u_i^{n+1}}{\partial x_i} = 0,$$

$$\frac{1}{\tau}\big[u_i^{n+1} - \mathtt{convect}\big(\mathbf{u}^n, -\tau, u_i^n\big)\big] + \frac{\partial p^{n+1}}{\partial x_i} - \mathrm{Sc}\Delta u_i^{n+1} + (\rho^n - 1)g^*\delta_{i2} = 0.$$

We proceed classically by multiplying these equations by appropriate test functions and then integrating on the whole domain Ω. The problem now is to determine the solution of the Navier-Stokes equations $(\mathbf{u}, p) \in V \times W$ such that for all $(\mathbf{v}, q) \in V \times W$ we have

$$\int_\Omega q^{n+1} \frac{\partial u_i^{n+1}}{\partial x_i} d\Omega = 0,$$

$$\frac{1}{\tau} \int_\Omega \left[u_i^{n+1} - \texttt{convect}(\mathbf{u}^n, -\tau, u_i^n) \right] v_i^{n+1} d\Omega$$

$$+ \int_\Omega \frac{\partial p^{n+1}}{\partial x_i} v_i^{n+1} d\Omega - \mathrm{Sc} \int_\Omega \Delta u_i^{n+1} v_i^{n+1} d\Omega + g^* \int_\Omega (\rho^n - 1) v_i^{n+1} \delta_{i2} d\Omega = 0.$$

The functional spaces V and W have to be compatible with the boundary conditions of the numerical problem. Here we choose the spaces

$$V = H_0^1(\Omega)^2, \quad W = \left\{ q \in L^2(\Omega) | \int_\Omega q \, d\Omega = 0 \right\}.$$

The choice of V and W obviously has an influence on the final form of the variational formulation. Here we have chosen to use the spaces, compatible with our problem, proposed by Hecht *et al.* in the FREEFEM++ tutorial [54]. The next step is to apply the Green's theorem to the momentum equation. The boundary conditions imposed to solve our numerical problem are then used to properly write the integrals along the boundary of the domain Γ. Indeed, the relationship obtained with the Green's theorem is valid for all test functions $v \in V = H_0^1(\Omega)$. Therefore, the product $\frac{\partial u_i}{\partial n} v_i$ resulting from the theorem is null all along the boundary of the domain. The momentum equation is then given for all test functions $\mathbf{v} \in V$ by

$$\frac{1}{\tau} \int_\Omega \left[u_i^{n+1} - \texttt{convect}(\mathbf{u}^n, -\tau, u_i^n) \right] v_i^{n+1} d\Omega + \int_\Omega \frac{\partial p^{n+1}}{\partial x_i} v_i^{n+1} d\Omega + \mathrm{Sc} \int_\Omega \nabla u_i^{n+1} \cdot \nabla v_i^{n+1} d\Omega$$

$$+ g^* \int_\Omega (\rho^n - 1) v_i^{n+1} \delta_{i2} d\Omega = 0.$$

Otherwise, the pressure term could be written for all $v \in V$,

$$\int_\Omega \frac{\partial p^{n+1}}{\partial x_i} v_i^{n+1} d\Omega = \int_\Omega \frac{\partial}{\partial x_i} \left(p^{n+1} v_i^{n+1} \right) d\Omega - \int_\Omega p^{n+1} \frac{\partial v_i^{n+1}}{\partial x_i} d\Omega.$$

However, the divergence theorem implies that

$$\int_\Omega \frac{\partial}{\partial x_i} \left(p^{n+1} v_i^{n+1} \right) d\Omega = \int_\Gamma p^{n+1} v_i^{n+1} n_i d\Omega = 0$$

because $v \in H_0^1(\Omega)^2$. Finally, the weak formulation of the Navier-Stokes equations is as follows: Determine the solutions $(\mathbf{u}, p) \in V \times W$ such that for all test functions $(\mathbf{v}, q) \in V \times W$ we have

$$\int_\Omega q^{n+1} \frac{\partial u_i^{n+1}}{\partial x_i} d\Omega = 0, \tag{A1}$$

$$\frac{1}{\tau} \int_\Omega \left[u_i^{n+1} - \texttt{convect}(\mathbf{u}^n, -\tau, u_i^n) \right] v_i^{n+1} d\Omega - \int_\Omega p^{n+1} \frac{\partial v_i^{n+1}}{\partial x_i} d\Omega$$

$$+ \mathrm{Sc} \int_\Omega \nabla u_i^{n+1} \cdot \nabla v_i^{n+1} d\Omega + g^* \int_\Omega (\rho^n - 1) v_i^{n+1} \delta_{i2} d\Omega = 0. \tag{A2}$$

The mass equation (A1) could be trivially subtracted from the momentum equation (A2). We have implemented this operation in the source code of FREEFEM++ in order to ensure the incompressibility condition. We have also subtracted a penalty term $\int_\Omega \varepsilon p^{n+1} q^{n+1} d\Omega$, where ε is a constant such that $\varepsilon \ll 1$. This term is imposed to improve the stability of the code by numerically

imposing the arbitrary constant in the pressure term. We have chosen $\varepsilon = 10^{-6}$ in our numerical simulations. There is no extra term in this weak formulation considering the boundary conditions of our numerical problem. Indeed, we only consider periodic boundary conditions for the velocity. This does not appear explicitly in the weak form, but is implemented in the FREEFEM++ source code through the choice of appropriate periodic finite elements.

c. Weak form of the advection-diffusion equation

As with the Navier-Stokes equation, we first write the temporal discretization of the advection-diffusion equation. This involves the density at times n and $n + 1$, and the velocity at time n. We have the discretized equation

$$\frac{1}{\tau}(\rho^{n+1} - \rho^n \circ X^n) - \Delta\rho^{n+1} = 0.$$

By using the same development as in the preceding section, we obtain, after the application of the Green's theorem, the equation involving the FREEFEM++ operator `convect` for all test functions $\xi \in X$,

$$\frac{1}{\tau}\int_\Omega [\rho^{n+1} - \texttt{convect}(\mathbf{u}^n, -\tau, \rho^n)]\xi^{n+1}d\Omega + \int_\Omega \nabla\rho^{n+1} \cdot \nabla\xi^{n+1}d\Omega - \int_\Gamma \frac{\partial\rho^{n+1}}{\partial n}\xi^{n+1}d\Gamma = 0,$$

where X is the Sobolev space H^1. Due to the periodic boundary condition and the condition of null flux at the bottom of the domain for the density, it only remains the contribution of the flux boundary condition at the solid surface in the surface integral of the previous equation. Along this last boundary the normal derivative is simply given by $\frac{\partial\rho}{\partial n} = \nabla\rho \cdot \mathbf{n} = -(\rho - \rho_m)$. The specific boundary condition modeling the dissolution is thus easily implemented. Finally, the weak formulation of the advection-diffusion equation is as follows: Determine the solution $\rho \in X$ such that for all test functions $\xi \in X$ we have

$$\frac{1}{\tau}\int_\Omega [\rho^{n+1} - \texttt{convect}(\mathbf{u}^n, -\tau, \rho^n)]\xi^{n+1}d\Omega + \int_\Omega \nabla\rho^{n+1} \cdot \nabla\xi^{n+1}d\Omega$$

$$+ \int_{\Gamma_{\text{solid}}} (\rho^{n+1} - \rho_m)\xi^{n+1}d\Gamma = 0. \tag{A3}$$

APPENDIX B: VALIDITY AND CONVERGENCE TESTS

For the canonical case of salt with $D = 10^{-9}$ m^2 s^{-1}, $\nu = 10^{-6}$ m^2 s^{-1}, $\alpha = 10^{-4}$ m s^{-1}, and $\beta = 0.2$, we checked that a small variation of the geometrical parameters (length L and height H) as well as of the numerical parameters (maximum time step $dt_{\max}$ and n_H a parameter characteristic of the mesh refinement) does not affect the general results. We chose as a quantitative measure the flux Φ, because it displays correctly when the system starts evolving away from the pure diffusion solution. Figure 12 shows that when we go away from the chosen parameters ($L = 1$ cm, $H = 2$ cm, $dt_{\max} = 0.01$, and $n_H = 50$) the simulations stay robust.

APPENDIX C: ONSET CHARACTERIZATION

In order to determine the onset time of solutal convection, we carefully examine the temporal evolution of the horizontal density profiles in the vicinity of the top boundary [as represented in Fig. 3(b)]. Before the convection starts, the stable diffusive concentration field is evolving in time [see Eq. (17)]. Thus, it is relevant to probe the horizontal density profile at an evolving vertical distance from the interface to track the density perturbations. To determine at which distance to probe the density, at each time of interest we compute a horizontally averaged vertical density profile $\langle\rho(z)\rangle_x$ and choose arbitrarily to look at the distance z_0 where $\langle\rho(z_0)\rangle_x = 0.8\langle\rho(0)\rangle_x$. Taking 50%, 80%, or a different arbitrary number does not change the results (data not shown).
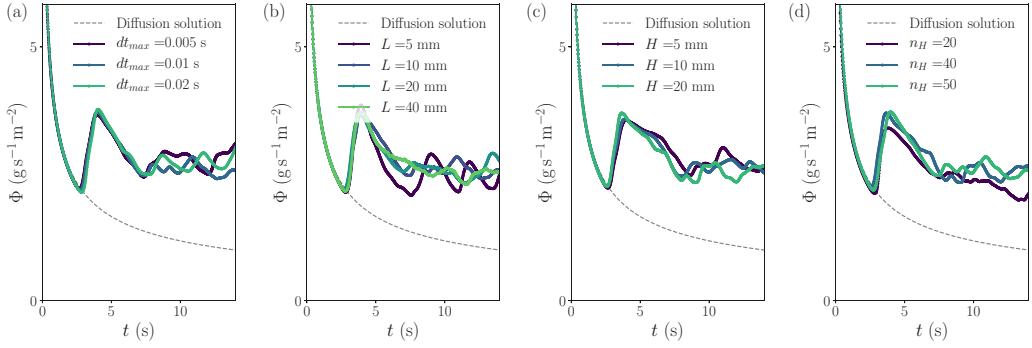
FIG. 12. Numerical robustness of the simulations. If not precised, all parameters are set to the case of the salt (see text). (a) Simulations for maximum time step dt_{max} varying from 0.005 s, to 0.01 s (typical value used for the canonical case) and 0.02s. No significant change is seen. (b) Length dependence, simulations are done for $L = 1$ cm which displays same behavior as $L = 2$ cm or $L = 0.5$ cm. (c) Height dependence, simulations are done for $H = 2$ cm which displays same behavior as $H = 1$ cm or $H = 0.5$ cm. (d) Mesh refining: the parameters n_H is characteristic of the refinement. For $n_H = 20$ the run is slightly different than for $n_H = 40$, but then, the same behavior is observed for $n_H = 50$ (chosen value for the canonical case).

We associate the amplitude of the instability with the standard deviation of the horizontal density profile: $\sigma(\rho_{z_0,t}) = \sqrt{\langle \rho(x, z_0, t)^2 \rangle_x - [\langle \rho(x, z_0, t) \rangle_x]^2}$. To determine the wavelength at a given time t and altitude z_0, we use standard autocorrelation techniques on the centered density profile $s(x) = \rho(x, z_0, t) - \langle \rho(x, z_0, t)(x) \rangle_x$.

The autocorrelation $A(x) = \int s(u)s(u + x)du$ has a central maximum peak in $x = 0$ whose amplitude $A(0)$ incidentally represents the variance of the original signal. The second maximum peak is at the typical wavelength λ of the central peak. The wavelength can also be determined from the position of the first minimum which stands between the central peak and the second peak. To determine the accuracy of the detection, we measure the associated score S, which is the amplitude of the second peak normalized by the amplitude of the central peak; $S := A(\lambda)/A(0)$. For one given run, by this method we extract at each time step the wavelength λ, measured from the position of the second maximum and the first minimum, as well as the score S and the standard deviation $\sigma(\rho_{z_0,t})$. This analysis clearly separates the three regimes.

As shown in Fig. 4, when $t < t_{onset}$, the wavelength is very small, hardly defined, and corresponds to a correlation score S close to zero. The standard deviation σ is very small. At a given time corresponding to t_{onset}, the wavelength sharply jumps to a larger and more defined value. We ascribe this jump to a marker of the onset of the instability and assign the value t_{onset} to this particular time.

In the precise case of salt in pure water, we find $t_{onset} = 1.02$ s. For $t > t_{onset}$, S increases towards values close to 1 and the rugosity increases exponentially. These features correspond to the second regime of instability development. The two estimations of the wavelength differ at the beginning of this regime, but converges towards a well-defined value.

At longer times, the standard deviation $\sigma(\rho_{z_0,t})$ saturates and fluctuates around a mean value. There we observe the emission of the sinking plumes (third regime). The transition between regimes (ii) and (iii) corresponds to the first emission of plumes. We define this transition time t_{em} as the time where the boundary layer δ is maximum ($t_{em} = 2.74$ s for pure water).

Note that, due to the increase of the thickness of the boundary layer as a function of time, the wavelength can evolve monotonically between t_{onset} and t_{em} and may not reach a constant value (see, for example, Fig. 13). In such a case, we define the wavelength at the onset as the average value between the wavelength at $t = t_{onset}$ and the one at $t = t_{em}$.
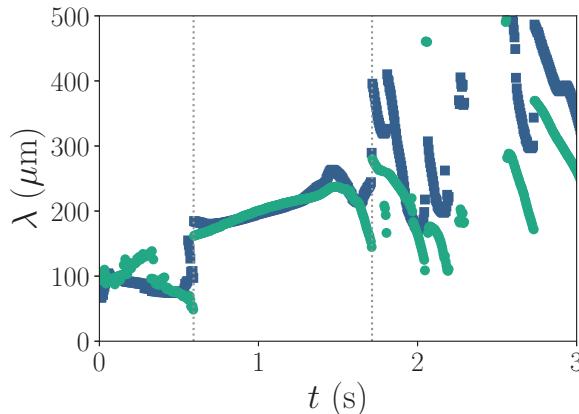
FIG. 13. Time evolution of the wavelength for parameters corresponding to the case of salt, but with an increased viscosity of $\nu = 2.9 \times 10^{-7}$ m^2 s^{-1}. The wavelength was determined by autocorrelation from the first minimum (green) and the first maximum (blue). Dotted vertical lines indicate the onset time and the plume emission time. Between these lines, the wavelength increases monotonically.

[1] P. Meakin and B. Jamtveit, Geological pattern formation by growth and dissolution in aqueous systems, Proc. R. Soc. A **466**, 659 (2010).

[2] *Karst Rock Features: Karren Sculpturing*, edited by A. Ginés, M. Knez, T. Slabe, and W. Dreybrodt (Založba ZRC, Ljubljana, 2009), Vol. 9.

[3] J. Colombani and J. Bert, Modelling karst geomorphology on different time scales, Geochim. Cosmochim. Acta **71**, 1913 (2007).

[4] S. L. Brantley, *Kinetics of Water-Rock Interaction* (Springer, Berlin, 2008).

[5] G. Kaufmann, Modelling karst geomorphology on different time scales, Geomorphology **106**, 62 (2009).

[6] F. Laouafa, J. Guo, and M. Quintard, Modeling of salt and gypsum dissolution: Applications, evaluation of geomechanical hazards, Eur. J. Environ. Civ. Eng., doi: 10.1080/19648189.2019.1579758 (2019).

[7] M. Fort, C. Chausse, N. Vanara, and G. Thomas, in *Landscapes and Landforms of France*, edited by M. Fort and M.-F. André (Springer Science + Business Media, Dordrecht, 2014), Chap. 2.

[8] K. H. Kang, H. C. Lim, H. W. Lee, and S. J. Lee, Evaporation-induced saline Rayleigh convection inside a colloidal droplet, Phys. Fluids **25**, 042001 (2013).

[9] J. Dunstan, K. J. Lee, Y. Hwang, S. F. Park, and R. E. Goldstein, Evaporation-driven convective flows in suspensions of nonmotile bacteria, Phys. Rev. Fluids **3**, 123102 (2018).

[10] L. Solari and G. Parker, Morphodynamic modeling of the basal boundary of ice cover on brackish lakes, J. Geophys. Res.: Earth **118**, 1432 (2013).

[11] J. A. Neufeld, M. A. Hesse, A. Riaz, M. A. Hallworth, H. A. Tchelepi, and H. E. Huppert, Convective dissolution of carbon dioxide in saline aquifers, Geophys. Res. Lett. **37**, L22404 (2010).

[12] H. E. Huppert and J. A. Neufeld, The fluid mechanics of carbon dioxide sequestration, Annu. Rev. Fluid Mech. **46**, 255 (2014).

[13] A. C. Slim, Solutal-convection regimes in a two-dimensional porous medium, J. Fluid Mech. **741**, 461 (2014).

[14] V. Loodts, C. Thomas, L. Rongy, and A. De Wit, Control of Convective Dissolution by Chemical Reactions: General Classification and Application to CO$_2$ Dissolution in Reactive Aqueous Solutions, Phys. Rev. Lett. **113**, 114501 (2014).

[15] D. Gechter, P. Ackerer P. Huggenberger, and H. Niklaus Waber, Genesis and shape of natural solution cavities within salt deposits, Water Resour. Res. **44**, W11409 (2008).

[16] C. Oltean, F. Golfier, and M. A. Bués, Numerical and experimental investigation of buoyancy-driven dissolution in vertical fracture, J. Geophys. Res.: Solid Ea. **118**, 2038 (2013).

[17] J. Schürr, Sur la vitesse de dissolution des sels dans leurs solutions aqueuses, J. Phys. Theor. Appl. **4**, 17 (1905).

[18] J. Schürr, Recherches sur la vitesse de dissolution des sels dans leurs solutions aqueuses, Ph.D. thesis, Clermont-Ferrand, 1905.

[19] F. H. Garner and J. M. Hoffman, Mass transfer from single solid spheres by free convection, AIChE J. **7**, 148 (1961).

[20] D. G. Thomas and R. A. Armistead, Concentration-gradient-driven convection: Experiments, Science **160**, 995 (1968).

[21] H. Grijseels, D. J. A. Crommelin, and C. J. de Blaey, Hydrodynamic approach to dissolution rate, Pharm. Weekblad **3**, 1005 (1981).

[22] S. Tait and C. Jaupart, Compositional convection in viscous melts, Nature (London) **338**, 571 (1989).

[23] S. Tait and C. Jaupart, Compositional convection in a reactive crystalline mush and melt differentiation, J. Geophys. Res.: Solid Ea. **97**, 6735 (1992).

[24] R. C. Kerr, Dissolving driven by vigorous compositional convection, J. Fluid. Mech. **280**, 287 (1994).

[25] T. S. Sullivan, W. J. Brown, M. D. Kerkel, and R. E. Ecke, Turbulent convection and surface patterning in solid dissolution, Phys. Lett. A **206**, 49 (1995).

[26] Y. Liu, L. Ning, and R. E. Ecke, Dynamics of surface patterning in salt-crystal dissolution, Phys. Rev. E **53**, R5572(R) (1996).

[27] T. S. Sullivan, Y. Liu, and R. E. Ecke, Turbulent solutal convection and surface patterning in solid dissolution, Phys. Rev. E **54**, 486 (1996).

[28] C. Cohen, M. Berhanu, J. Derr, and S. Courrech du Pont, Erosion patterns on dissolving and melting bodies, Phys. Rev. Fluids **1**, 050508 (2016).

[29] C. Cohen, M. Berhanu, J. Derr, and S. Courrech du Pont, Erosion patterns on dissolving and melting bodies (unpublished).

[30] M. S. Davies Wykes, J. M. Huang, G. A. Hajjar, and L. Ristroph, Self-sculpting of a dissolvable body due to gravitational convection, Phys. Rev. Fluids **3**, 043801 (2018).

[31] T. D. Foster, Stability of a homogeneous fluid cooled uniformly from above, Phys. Fluids **8**, 1249 (1965).

[32] I. G. Currie, The effect of heating rate on the stability of stationary fluids, J. Fluid Mech. **29**, 337 (1967).

[33] T. D. Foster, Effect of boundary conditions on the onset of convection, Phys. Fluids **11**, 1257 (1968).

[34] G. M. Homsy, Global stability of time-dependent flows: Impulsively heated or cooled fluid layers, J. Fluid Mech. **60**, 129 (1973).

[35] J. Ennis-King, I. Preston, and L. Paterson, Onset of convection in anisotropic porous media subject to a rapid change in boundary conditions, Phys. Fluids **17**, 084107 (2005).

[36] C. K. Choi, J. H. Park, M. C. Kim, J. D. Lee, J. J. Kim, and E. J. Davis, The onset of convective instability in a horizontal fluid layer subjected to a constant heat flux from below, Int. J. Heat Mass Transf. **47**, 4377 (2004).

[37] C. F. Ihle and Y. Nino, The onset of nonpenetrative convection in a suddenly cooled layer of fluid, Int. J. Heat Mass Transf. **49**, 1442 (2006).

[38] A. C. Slim and T. S. Ramakrishnan, Onset and cessation of time-dependent, dissolution-driven convection in porous media, Phys. Fluids **22**, 124103 (2010).

[39] F. Doumenc, T. Boeck, B. Guerrier, and M. Rossi, Transient Rayleigh-Bénard-Marangoni convection due to evaporation: A linear non-normal stability analysis, J. Fluid Mech. **648**, 521 (2010).

[40] O. S. Kerr and Z. Gumm, Thermal instability in a time-dependent base state due to sudden heating, J. Fluid Mech. **825**, 1002 (2017).

[41] M. Alkattan, E. H. Oelkers, J.-L. Dandurand, and J. Schott, Experimental studies of halite dissolution kinetics, 1 the effect of saturation state and the presence of trace metals, Chem. Geol. **137**, 201 (1997).

[42] G. Lanaro and G. N. Patey, Molecular dynamics simulation of NaCl dissolution, J. Phys. Chem. B **119**, 4275 (2015).

[43] H. B. Aaron and G. R. Kotler, The effects of curvature on the dissolution kinetics of spherical precipitates, Met. Sci. J. **4**, 222 (1970).

[44] M. Enomoto and N. Nojiri, Influence of interfacial curvature on the growth and dissolution kinetics of a spherical precipitate, Scripta Mater. **36**, 625 (1997).

[45] S. Chandrasekhar, *Hydrodynamic and Hydromagnetic Stability* (Clarendon, Oxford, 1961).

[46] M. C. Kim and S. G. Lee, Onset of solutal convection in liquid phase epitaxy system, Korean J. Chem. Eng. **26**, 21 (2009).

[47] *The Handbook of Chemistry and Physics*, edited by D. R. Lide (CRC, Boca Raton, 2004).

[48] V. Vitagliano and P. A. Lyons, Diffusion coefficients for aqueous solutions of sodium chloride and barium chloride, J. Am. Chem. Soc. **78**, 1549 (1956).

[49] W. V. R. Malkus, The heat transport and spectrum of thermal turbulence, Proc. R. Soc. London Ser. A **225**, 196 (1954).

[50] R. C. Kerr, Melting driven by vigorous compositional convection, J. Fluid. Mech. **280**, 255 (1994).

[51] Q. M. Sharif, M. Hussain, and M. T. Hussain, Chemical evaluation of a major salt deposits of Pakistan, J. Chem. Soc. Pakistan **29**, 569 (2007).

[52] A. Lo Surdo, E. M. Alzola, and F. J. Millero, The (p, V, T) properties of concentrated aqueous electolytes, J. Chem. Thermodyn. **14**, 649 (1982).

[53] F. Hecht, New development in freefem++, J. Numer. Math. **20**, 251 (2012).

[54] F. Hecht, S. Auliac, O. Pironneau, J. Morice, A. Le Hyaric, K. Ohtsuka, and P. Jollier, Freefem++, 2018, available at http://www3.freefem.org/ff++/ftp/freefem++doc.pdf.

[55] See Supplemental Material at http://link.aps.org/supplemental/10.1103/PhysRevFluids.4.103801 for a video.

[56] J. Crank, *The Mathematics of Diffusion* (Clarendon, Oxford, 1975).

[57] H. R. Brown, Rayleigh-Taylor instability in a finite thickness layer of a viscous fluid, Phys. Fluids A **1**, 895 (1988).

[58] L. Limat, Instabilité d'un liquide suspendu sous un surplomb solide: influence de l'épaisseur de la couche, C. R. Acad. Sci. II B **317**, 563 (1993).

[59] J. R. Lister and R. C. Kerr, The effect of geometry on the gravitational instability of a buoyant region of viscous fluid, J. Fluid. Mech. **202**, 577 (1989).

[60] J. J. Hidalgo, M. Dentz, Y. Cabeza, and J. Carrera, Dissolution patterns and mixing dynamics in unstable reactive flow, Geophys. Res. Lett. **42**, 6357 (2015).

[61] B. Rabbanipour Esfahani, S. C. Hirata, S. Berti, and E. Calzavarini, Basal melting driven by turbulent thermal convection, Phys. Rev. Fluids **3**, 053501 (2018).

[62] B. Favier, J. Purseed, and L. Duchemin, Rayleigh-Bénard convection with a melting boundary, J. Fluid Mech. **858**, 437 (2019).

[63] G. Kaufmann and W. Dreybrodt, Calcite dissolution kinetics in the system $CaCO_3$-H_2O-CO_2 at high undersaturation, Geochim. Cosmochim. Acta **71**, 1398 (2007).

[64] H. Luo, F. Laouafa, G. Debenest, and M. Quintard, Large scale cavity dissolution: From the physical problem to its numerical solution, Eur. J. Mech. B **52**, 131 (2015).

[65] J. Guo, F. Laouafa, and M. Quintard, A theoretical and numerical framework for modeling gypsum cavity dissolution, Int. J. Numer. Anal. Meth. Geomech. **40**, 1662 (2016).

[66] K. R. Moore, H. M. Holländer, M. Basri, and M. Roemer, Application of geochemical and groundwater data to predict sinkhole formation in a gypsum formation in Manitoba, Canada, Environ. Earth Sci. **78**, 193 (2019).

[67] Available at http://www.freefem.org/

[68] R. Temam, *Navier-Stokes Equations: Theory and Numerical Analysis* (North-Holland, Amsterdam, 1979), Vol. 2.

[69] W. Layton, *Introduction to the Numerical Analysis of Incompressible Viscous Flows* (Society for Industrial and Applied Mathematics, Philadelphia, 2008).